American Mineralogist, Volume 92, pages 811–828, 2007

Intercalibration of FTIR and SIMS for hydrogen measurements in glasses and nominally anhydrous minerals

Cyril Aubaud,[1,3,*] Anthony C. Withers,[1] Marc M. Hirschmann,[1] Yunbin Guan,[2] Laurie A. Leshin,[2] Stephen J. Mackwell,[3] and David R. Bell[4]

[1]Department of Geology and Geophysics, University of Minnesota, 108 Pillsbury Hall, 310 Pillsbury Drive, Minneapolis, Minnesota 55455, U.S.A.
[2]Department of Geology, Arizona State University, Box 871404, Tempe, Arizona 85287-1404, U.S.A.
[3]Lunar and Planetary Institute, 3600 Bay Area Boulevard, Houston, Texas 77058, U.S.A.
[4]Department of Chemistry and Biochemistry, Arizona State University, Tempe, Arizona 85282, U.S.A.

Abstract

We present new Fourier Transform Infrared Spectroscopy (FTIR) and ion microprobe/secondary ion mass spectrometry (SIMS) analyses of ^{1}H in 61 natural and experimental geological samples. These samples include 8 basaltic glasses (0.17 to 7.65 wt% H_2O), 11 rhyolitic glasses (0.143 to 6.20 wt% H_2O), 17 olivines (~0 to 910 wt. ppm H_2O), 9 orthopyroxenes (~0 to 263 wt. ppm H_2O), 8 clinopyroxenes (~0 to 490 wt. ppm H_2O), and 8 garnets (~0 to 189 wt. ppm H_2O). By careful attention to vacuum quality, the use a Cs^+ primary beam, and a resin-free mounting technique, we routinely achieve hydrogen backgrounds equivalent to less than 5 ppm by weight H_2O in olivine. Compared to previous efforts, the new calibration extends to a wider range of H_2O contents for the minerals and is more reliable owing to a larger number of standards and to characterization of anisotropic minerals by polarized FTIR on oriented crystals. When observed, discrepancies between FTIR and SIMS measurements are attributable to inclusions of hydrous minerals or fluid inclusions in the crystals. Inclusions more commonly interfere with FTIR analyses than with SIMS, owing to the much larger volume sampled by the former. Plots of H_2O determined by FTIR vs. (^{1}H/^{30}Si) × (SiO_2), determined by SIMS and electron microprobe (EMP) yield linear arrays and for each phase appear to be insensitive to bulk composition. For example, basalt and rhyolite calibration slopes cannot be distinguished. On the other hand, calibration slopes of different phases vary by up to a factor of 4. This reflects either phase-specific behavior of ^{1}H/^{30}Si secondary ion ratios excited by Cs^+ ion beams or discrepancies between phase-specific FTIR absorption coefficient schemes.

Keywords: Spectroscopy, infrared, water, mantle, ion microprobe

Introduction

Hydrogen incorporated in nominally anhydrous minerals (NAMs) influences mantle physical and chemical properties including rheology (e.g., Hirth and Kohlstedt 1995), seismic wave propagation (Karato and Jung 1998; Katayama et al. 2004), electrical conductivity (Huang et al. 2005; Karato 1990), chemical diffusivity (Wang et al. 2004), and both the locus and kinetics of subsolidus phase transitions (Kubo et al. 1998; Wood 1995). Hydrogen also has a significant influence on the location and extent of partial melting (Asimow et al. 2004; Hirschmann 2006; Hirth and Kohlstedt 1996). It is therefore important to quantify experimentally the relationship between hydrogen concentrations in minerals and melts and physical and chemical properties.

Such experimental constraints are only meaningful if hydrogen concentrations and speciation in the phases (minerals and melt) can be precisely and accurately determined. Many analytical techniques for absolute measurements of hydrogen in glasses or minerals are available but each of these has their advantages and disadvantages. Manometry is easily available but is destructive and requires large samples, which remains problematic in the case of NAMs. Techniques using nuclear facilities (NRRA, ERDA) have been shown to be useful (Bell et al. 2003; Sweeney et al. 1997) but remain of limited practical use because of limited access. Also, spectroscopic methods such as NMR (e.g., Kohn 1996) are problematic to use for hydrogen determinations when iron is present in the matrix.

Among the techniques used to determine H_2O concentrations in mantle minerals and in quenched silicate melts, Fourier transform infrared spectroscopy (FTIR) may be the most powerful because it provides information about both bulk concentration and local bonding environments. However, FTIR has several disadvantages, particularly for analyzing the small crystals produced in many high-pressure experiments. Such limitations are particularly evident when the crystals produced in these experiments are optically anisotropic, as these require polarized FTIR observations along three directions of the indicatrix to make accurate quantitative H_2O measurements (Libowitzky and Rossman

---

* Present address: Institut de Physique du Globe de Paris, Laboratoire de Géochimie des Isotopes Stables, 2 Place Jussieu, 75251 Paris Cedex 05, France. E-mail: aubaud@ipgp.jussieu.fr

0003-004X/07/0506–811$05.00/DOI: 10.2138/am.2007.2248

1996). In some cases, this can be overcome by using polarized measurements in random orientations and mathematically correcting for misorientation (Asimow et al. 2004).

Secondary Ion Mass Spectrometry (SIMS) holds considerable promise for routine analysis of H in crystals produced in experiments. Hydrogen measurement by SIMS has the advantage of high spatial resolution and insensitivity to crystal orientation, but must be calibrated against an appropriate set of standards (Koga et al. 2003). A serious shortcoming of early hydrogen measurements using SIMS was a relatively high hydrogen background that impeded measurement of low hydrogen concentrations (<100 ppm wt. H_2O, e.g., Deloule et al. 1995; Hinthorne and Andersen 1975; Ihinger et al. 1994; Yurimoto et al. 1989). However, several methodological developments described by Koga et al. (2003) allow low-blank hydrogen measurements in nominally anhydrous minerals (NAMs) by SIMS using a Cs^+ primary beam and careful attention to vacuum quality along with a resin-free mounting technique in which samples are pressed into Al disks filled with indium metal. However, this pioneering study relied on a less than ideal set of standards. For example, the olivine and orthopyroxene standards were characterized by FTIR using unpolarized measurements and the calibration of Paterson (1982). As a consequence, comparison of these standards to H measured by SIMS required arbitrary readjustment of the concentrations inferred from FTIR. Further, the distribution of concentrations in available standards left some ambiguity regarding comparison of FTIR and SIMS observations. This was particularly true for clinopyroxene, for which only one sample was available.

Another important consideration regarding SIMS measurements of H is the possible influence of matrix composition on the intensity of observed secondary H ion beams. Previous studies suggest the existence of such matrix effects, though results have varied depending on analytical conditions and on the treatment of data. Hinthorne and Andersen (1975) calibrated measurement of H by SIMS for stoichiometric OH-bearing minerals using an $^{16}O^-$ primary beam. Although some scatter was observed, all standards investigated defined a straight line in a plot of H vs. $(H^+/Si^+)_{SIMS} \times (Si)_{EMP}$, suggesting small matrix effects. In contrast, an investigation of albitic, granitic, and anorthitic glasses by Deloule et al. (1995) revealed a marked compositional dependence to the slope of calibration lines in a plot $(H^+/Si^+)_{SIMS}$ vs. $(H/Si)_{sample}$. Similar observations have been made by others for a range of glass compositions, ion microprobe instrumentation, and primary ion beams (Hauri et al. 2002; Ihinger et al. 1994; King et al. 2002; Sobolev and Chaussidon 1996). In particular, King et al. (2002) showed a correlation between volatile-free molar weight and the slope of the SIMS working curve for a comprehensive suite of H-rich glasses and minerals. For NAMs, Koga et al. (2003) noted that the working curve slope applicable to garnet differed from those for olivine and pyroxene, possibly owing to a compositional effect. Koga et al. (2003) also found an apparent correlation between SIMS working curve slopes and FeO contents of the phases examined, though this correlation did not extend to garnet.

Here we present a new FTIR-SIMS cross-calibration of hydrogen measurements for basaltic glass, rhyolitic glass, olivine, orthopyroxene, clinopyroxene, and garnet. Our observations are based on a larger set of standards than investigated previously, with more extensive polarized FTIR observations.

THE STANDARDS

Some of the standards investigated are natural and experimental samples for which H_2O concentrations were determined in previous studies, as detailed in Table 1. Major element compositions of these samples are listed in Table 2 and accepted H_2O concentrations and source references are given in Table 3. We also synthesized or annealed many new samples. The sources of these samples, their major element compositions, and their H_2O contents (previously published or newly determined) are also listed in Tables 1–3. Additionally, details of their synthesis and quantitative infrared spectroscopic characterization are elaborated below.

EXPERIMENTAL METHODS

Dry minerals

We experimentally dehydrated a natural orthopyroxene from Bamble (Norway) and a natural garnet from the Navajo Nation (Colorado Plateau, Arizona, U.S.A.), both obtained from Wards Natural Science, Inc. These samples were heated at 1000 °C for 72 h in a one atmosphere furnace in a CO_2/CO gas stream adjusted to an oxygen fugacity one order of magnitude more reducing than the quartz-fayalite-magnetite buffer. Unpolarized infrared spectroscopy on thick (>1 mm) doubly polished crystal slabs show that the resulting crystals are effectively anhydrous, with H_2O contents below the detection limit of the FTIR instrument (<1 wt. ppm).

High-pressure experiments

High water content basalts and olivines of variable H_2O concentration were generated by annealing at high pressure in an end-loaded piston cylinder using the methods and calibration described in Xirouchakis et al. (2001).

High-water content basaltic glasses

High-water content basalts were synthesized from a natural basaltic glass that derives from the mid-Atlantic ridge at 25°N (V25-RD1-T1C, Miyashiro et al. 1969) and was provided to us by D.L. Kohlstedt. A new major element composition obtained by electron microprobe (see Analytical Methods section below) in glass AC74 (Table 4) is similar to that published previously by Miyashiro et al. (1969). Approximately 15 mg of fine-grained (<3 μm) basalt powder was loaded with varying amounts of distilled water in $Au_{75}Pd_{25}$ 3 mm capsules that were then welded shut. Run conditions are shown in Table 5. The quench rate in this device is 75 °C/s for the first 10 s of quenching, so that the resulting charges consist only of clear brown glass without any vesicles, quench crystals or minerals. The amount of water measured by infrared spectroscopy (methods described in analytical methods section below) in the resulting glasses is broadly similar to the amount of water loaded in the capsule (Tables 3 and 5).

Experimentally hydrated olivines

San Carlos olivine crystals (~Fo90, Table 2) with an initial H_2O concentration of less than 1 ppm (Table 3) were used as starting materials for these experiments. In initial experiments, cubes of oriented single crystals were used. However, these produced aggregates of spherical olivine grains ~30 μm in diameter with random orientation, which were not suitable for polarized infrared spectroscopy. We surmised that the sharp edges of the initial grains represented high-energy surfaces that promoted recrystallization. Therefore, in subsequent experiments, we used unoriented spherical single crystals of olivine about 2 mm in diameter. These were prepared in a Bond mill (Bond 1951). Optical examination under crossed polars verified that these experiments produced large single crystals, although some cracks resulted from quenching and decompression.

Compositions of starting materials and run conditions for these experiments are in Tables 4 to 6. Several different types of olivine hydration experiments were conducted:

(1) Experiments at 1000 and 1100 °C, in which the olivines were surrounded with either brucite (AC84), San Carlos olivine powder and free water (AC85), or powder made from crystals of the Kenyan enstatite (Mix1; Table 4) and free water (AC56 and AC58).

(2) Experiments at 1300 °C, in which the olivines were surrounded by a powdered mixture of San Carlos olivine and Bamble orthopyroxene (Mix2; Table 4) and

TABLE 1. List of the standards analyzed in this study

Sample	Location	References
Basaltic glasses		
ALV519-4-1	East Pacific Rise	1, 2
JdFD10	Juan de Fuca Ridge	3
KN54Sta52	Cayman trough	3
KN54Sta51	Cayman trough	3
AC49	experimental	3
AC46	experimental	3
AC47	experimental	3
AC50	experimental	3
Rhyolitic glasses		
Red Hill Cinder Cone	California, U.S.A.	3
EDF natural	Erevan Dry Fountain, Armenia	4
EDF1(E)	experimental	4
EDF1(H)	experimental	4
EDF2	experimental	4
EDF2.4	experimental	4
EDF3	experimental	4
EDF4	experimental	4
EDF4b	experimental	4
EDF5	experimental	4
EDF6	experimental	4
Olivine crystals		
ROM177	Monastery Kimberlite, South Africa	5
ROM250 OL2	Monastery Kimberlite, South Africa	5
ROM250 OL13	Monastery Kimberlite, South Africa	5
AC90	experimental	3
AC93	experimental	3
AC86	experimental	3
Fo100	experimental	3
Damaping OL	Damaping, China	3
Ant Hill OL	Navajo Nation, Colorado Plateau, AZ, U.S.A.	3
San Carlos OL	San Carlos, AZ, U.S.A.	3
AC56	experimental	3
AC58	experimental	3
AC84	experimental	3
AC85	experimental	3
AC89	experimental	3
AC87	experimental	3
AC94	experimental	3
Orthopyroxene crystals		
Bamble Dry	experimental	3
San Carlos OPX	San Carlos, AZ, U.S.A.	3
Bamble	Norway	3
Damaping OPX	Damaping, China	3
India	Kangan, Andhra-Pradesh, India	3, 6
Kenya	Sultan Hamud, Kenya	3, 6
KBH-1	Kilbourne Hole, New Mexico	7
ROM273-OG2	Monastery Kimberlite, South Africa	5
Clinopyroxene crystals		
PMR53HT	experimental	7
Dish Hill	Dish Hill, Siberia Crater, California	3
Damaping CPX	Damaping, China	3
Tunguska	Tungunska, Russia	3
ROM271 DI10	Monastery Kimberlite, South Africa	5
PMR53	Premier Mine, South Africa	7
ROM271 DI16	Monastery Kimberlite, South Africa	5
ROM271 DI21	Monastery Kimberlite, South Africa	5
Garnet crystals		
Ant Hill Dry	experimental	3
ROM263 GT52	Monastery Kimberlite, South Africa	5
ROM263 GT25	Monastery Kimberlite, South Africa	5
ROM263 GT09	Monastery Kimberlite, South Africa	5
Dora Maira	Parigi, Western Alps, Italy	3, 8
MON9GT	Monastery Kimberlite, South Africa	5
Ant Hill Clear	Navajo Nation, Colorado Plateau, AZ, U.S.A.	3
Ant Hill Dark	Navajo Nation, Colorado Plateau, AZ, U.S.A.	3

Notes: References for the source of the standards: 1 = Bryan and Moore (1977); 2 = Fine and Stolper (1985/1986); 3 = This study; 4 = Withers and Behrens (1999); 5 = Bell et al. (2004); 6 = Koga et al. (2003); 7 = Bell et al. (1995); 8 = Chopin (1984).

free water (runs AC86, AC90, AC93);

(3) Experiments at 1300 °C, in which the olivines were surrounded by a synthetic (Mg,Fe)O powder of composition 46.9 wt% MgO and 52.7 wt% FeO (Mix3; Table 4) and free water (runs AC87, AC89, AC94). The (Mg,Fe)O was prepared from a mix of MgO, Fe and Fe_2O_3 equilibrated for 24 h at 1 atm, 1100 °C and a f_{O_2} of 10^{-12} atm; i.e., between the IW and WM buffers to ensure that essentially all iron was ferrous. The composition was chosen to yield crystals of ferropericlase (after experiments) in Fe–Mg equilibrium with an olivine of composition Fo_{90} (Matveev et al. 2001; Nafziger and Muan 1967; Suzuki et al. 1996; Wiser and Wood 1991).

The last two series were designed to reproduce the results of Matveev et al. (2001), who found markedly different FTIR spectra for olivines equilibrated at different activities of SiO_2, indicating that at least one of the defect associates involves hydrogen ions and silicon vacancies. These runs were conducted at relatively high temperature to promote equilibrium populations of silicon and metal vacancies (e.g., Mackwell et al. 1988).

ANALYTICAL METHODS

Electron microprobe analysis

Major element analyses of glasses and minerals were performed by wavelength-dispersive electron microprobe analysis with the JEOL JXA8900R at the University of Minnesota, using an acceleration voltage of 15 kV, beam currents of 20 nA for minerals, 10 nA for basaltic glasses and 2 nA for rhyolitic glasses, and ZAF data reduction with software supplied by JEOL. A focused beam (1–2 μm diameter) was used for minerals, and a beam diameter of 30 μm was used for glasses. The counting time was 10 s for each element and 5 s for the background. Glass and mineral standards from Jarosewich et al. (1980) were used. During each session the unknowns were analyzed between standards as a check for drift. Uncertainties are reported as 1σ standard deviation of *n* analyses and are listed along with the results (Tables 2 and 4).

Fourier transformed infrared spectroscopy

Water contents of the glasses and the crystals were measured by Fourier Transform Infrared Spectroscopy (FTIR). For the isotropic glasses and garnet crystals, analyses were based on unpolarized infrared spectra. As discussed by Libowitzky and Rossman (1996), rigorous quantitative analysis of anisotropic crystals involves summing absorption intensities from polarized spectra in all three vibration directions. Therefore, olivine, orthopyroxene, and clinopyroxene crystals were analyzed by polarized infrared spectroscopy on oriented crystals. In all cases, infrared spectra were acquired in transmission mode.

The water content (expressed as weight percent or ppm H_2O) was calculated with the Beer-Lambert law of the general form:

$$C_{H_2O} = \frac{M_{H_2O} \times A}{\rho \times d \times \varepsilon} \tag{1}$$

where M_{H_2O} is the molecular weight of H_2O (18.02 in g mol^{-1}), A denotes the absorbance (peak height in the case of the glasses or integrated area in the case of the minerals), ρ the density in g l^{-1}, d the thickness in cm, and ε is the molar absorption coefficient (linear molar absorption coefficient in l mol^{-1} cm^{-1} in the case of the peak height method or integral molar absorption coefficient in l mol^{-1} cm^{-2} in the case of the integrated area method).

Sample preparation

Samples were cut with a wire saw (WS-22 Princeton Corp.) equipped with a 50 μm thick tungsten wire and polished with diamond lapping films of decreasing grain size (30, 9, 3, 1 μm). Final polishing was made either with Syton colloidal silica or a 1 μm alumina suspension.

Crystal orientation and thickness

Olivine, orthopyroxene, and clinopyroxene crystals were oriented with a microscope by observing the position of extinction under crossed polars. Uncertainties in orientation of the samples are less than 10° and generally better than 5°, which is the accepted uncertainty on the crystals used in the calibrations for olivine, orthopyroxene and clinopyroxene crystals (Bell et al. 1995; Bell et al. 2003). For olivine, identification of the indicatrix axes was made by observing the silicate network absorption bands located between 1200 and 2200 cm^{-1} following Lemaire et al. (2004) and Asimow et al. (2006). Sample thicknesses were measured with a Mitutoyo digital micrometer with an uncertainty of ±1 μm.

TABLE 2. Major element composition of the standards

Sample	SiO_2 (wt%)	TiO_2 (wt%)	Al_2O_3 (wt%)	Cr_2O_3 (wt%)	FeO* (wt%) †	MnO (wt%)	MgO (wt%)	CaO (wt%)	Na_2O (wt%)	K_2O (wt%)	H_2O (wt%)	Total (wt%)	Ref. Major elements	Ref. H_2O content
Basaltic glasses														
ALV519-4-1	49.07	0.74	16.44	0.03	8.86	0.16	10.15	11.65	2.13	0.07	0.17	99.47	1	7
JdFD10	50.11	1.83	13.76		11.70	0.18	6.92	11.10	2.70	0.20	0.348	98.85	2	2
KN54Sta52	50.81	2.49	14.73		10.30	0.17	5.77	9.49	3.79	0.35	0.495	98.38	2	2
KN54Sta51	50.68	1.79	15.78		8.83	0.16	6.99	10.32	3.57	0.26	0.647	99.02	2	2
AC49	49.57	1.67	15.72		8.59		7.37	10.43	2.95	0.25	1.98	98.52	2	2
AC46	48.66	1.60	15.49		8.54		7.56	10.24	2.88	0.23	3.91	99.10	2	2
AC47	47.40	1.50	15.06		8.57		7.53	10.08	2.70	0.22	6.03	99.09	2	2
AC50	47.32	1.51	14.75		8.53		7.04	9.67	2.68	0.23	7.65	99.38	2	2
Rhyolitic glasses														
Red Hill Cinder Cone	76.59	0.06	12.67	0.04	1.05	0.06	0.02	0.43	3.55	4.66	0.143	99.27	2	2
EDF natural	77.04	0.11	12.76		0.68	0.07	0.08	0.58	4.07	4.79	0.23	100.41	2	2
EDF1(E)	76.16	0.11	12.61		0.67	0.07	0.08	0.57	4.02	4.74	0.968	100.00	3	3
EDF1(H)	75.61	0.11	12.52		0.67	0.07	0.08	0.57	3.99	4.70	1.682	100.00	3	3
EDF2	75.27	0.11	12.47		0.66	0.07	0.08	0.57	3.98	4.68	2.116	100.00	3	3
EDF2.4	74.79	0.11	12.39		0.66	0.07	0.08	0.56	3.95	4.65	2.741	100.00	3	3
EDF3	74.27	0.11	12.30		0.66	0.07	0.08	0.56	3.92	4.62	3.423	100.00	3	3
EDF4	73.75	0.11	12.22		0.65	0.07	0.08	0.56	3.90	4.59	4.099	100.00	3	3
EDF4b	73.67	0.11	12.20		0.65	0.07	0.08	0.56	3.89	4.58	4.202	100.00	3	3
EDF5	72.94	0.10	12.08		0.64	0.07	0.08	0.55	3.85	4.54	5.158	100.01	3	3
EDF6	72.13	0.10	11.95		0.64	0.07	0.08	0.54	3.81	4.49	6.201	100.00	3	3
Olivine crystals														
ROM177	38.87	0.02	0.001	0.006	17.71	0.13	43.93	0.04	0.01	0.00	0.0125	100.73	4	4
ROM250 OL2	39.16	0.04	0.033	0.002	14.44	0.20	46.01	0.08	0.03	0.00	0.0183	100.01	4	4
ROM250 OL13	38.61	0.02	0.001	0.002	19.09	0.18	42.84	0.05	0.01	0.00	0.0243	100.82	4	4
AC90 core	42.03	0.01	0.01		9.40	0.13	49.15	0.02	0.03	0.03	0.0079	101.20	2	2
AC90 rim	42.19	0.00	0.01		7.73	0.11	50.91	0.03	0.01	0.03	–	101.44	2	2
AC93	41.45	0.01	0.04		8.68	0.12	50.34	0.06	0.01	0.02	0.0068	101.09	2	2
AC86	41.07	0.00	0.01		6.89	0.10	51.28	0.02	0.00	0.02	0.0073	99.75	2	2
Fo100	42.70	0.00	0.00		0.00		57.30	0.00	0.00	0.00	0	100.00	2	5
Damaping OL	40.77	0.01	0.02		9.1	0.12	49.33	0.06	0.01	0.03	0.0001	99.45	2	2
Ant Hill OL	40.54	0.00	0.01		7.74	0.10	50.94	0.01	0.04	0.04	0.0009	99.42	2	2
San Carlos OL	41.37	0.01	0.02		9.48	0.14	49.22	0.08	0.02	0.02	0.0001	100.37	2	2
AC56	39.98	0.01	0.00		8.27	0.12	50.55	0.08	0.06	0.04	0.0064	99.48	2	2
AC58	40.22	0.01	0.02		8.66	0.12	49.57	0.08	0.05	0.05	0.0048	99.17	2	2
AC84 core	41.21	0.01	0.01		9.34	0.13	49.33	0.08	0.01	0.01	0.0052	100.50	2	2
AC84 rim	39.78	0.00	0.03		0.79	0.02	59.33	0.01	0.01	0.03		100.00	2	2
AC85	40.04	0.00	0.00		9.51	0.14	49.18	0.05	0.01	0.02	0.0084	99.33	2	2
AC89 core	40.97	0.02	0.02		9.55	0.13	49.61	0.08	0.02	0.03	–	100.82	2	2
AC89 rim	41.79	0.00	0.10		3.67	0.03	54.83	0.00	0.00	0.03	0.0271	100.46	2	2
AC87	40.57	0.01	0.01		9.32	0.13	49.87	0.05	0.01	0.02	0.0478	100.41	2	2
AC94 rim	42.36	0.03	0.00	0.00	4.19	0.00	53.09	0.04	0.00	0.04	0.0910	99.88	2	2
AC94 core	41.53	0.01	0.06	0.03	9.33	0.20	48.83	0.05	0.00	0.02	–	100.44	2	2
Orthopyroxene crystals														
Bamble Dry	56.03	0.09	2.73	0.41	5.61	0.10	34.53	1.23	0.12	0.01	0	100.86	2	2
San Carlos OPX	56.66	0.02	1.89	0.42	5.07	0.13	35.20	0.80	0.09	0.03	0.0038	100.32	2	2
Bamble	57.27	0.03	2.03	0.30	4.78	0.09	35.53	0.79	0.09	0.02	0.0055	100.92	2	2
Damaping OPX	55.44	0.04	4.22	0.37	6.22	0.10	33.92	0.53	0.05	0.02	0.0078	100.91	2	2
India	54.52	0.00	1.91		13.43		30.15	0.00	0.00	0.00	0.0141	100.02	5	2
Kenya	57.24	0.00	0.00		8.63		34.12	0.00	0.00	0.00	0.0147	100.01	5	2
ROM167	56.96	0.16	0.72	0.00	10.64	0.18	31.31	0.80	0.18	0.00	0.0215	100.97	4	4
KBH-1	54.68	0.11	4.73	0.49	5.88	0.14	32.92	0.86	0.12	0.00	0.0217	99.95	6	6
ROM273-OG2	57.37	0.21	1.29	0.13	7.20	0.13	32.60	1.52	0.31	0.00	0.0263	100.79	4	4
Clinopyroxene crystals														
PMR53HT	54.78	0.35	2.83	0.14	6.87	0.14	18.30	13.26	2.13	0.05	0	98.85	6	6
Dish Hill	47.90	1.52	9.46	0.01	7.30	0.13	13.93	18.75	0.99	0.02	0	100.00	2	2
Damaping CPX	52.64	0.33	6.01	0.86	2.25	0.07	15.52	20.85	1.47	0.01	0.0178	100.02	2	2
Tungunska	55.27	0.06	0.20	0.53	1.05	0.06	18.23	24.73	0.26	0.01	0.0106	100.39	2	2
ROM271 DI10	55.32	0.14	0.55	0.30	5.08	0.10	16.20	21.35	1.29	0.01	0.0195	100.35	4	4
PMR53	54.78	0.35	2.83	0.14	6.87	0.14	18.30	13.26	2.13	0.05	0.0268	98.88	6	6
ROM271 DI16	55.82	0.33	2.46	0.30	5.51	0.12	20.78	13.78	1.54	0.02	0.0439	100.71	4	4
ROM271 DI21	55.09	0.49	2.54	0.20	6.04	0.13	19.02	14.93	1.78	0.02	0.0490	100.29	4	4
Garnet crystals														
Ant Hill Dry	40.93	0.09	21.90	2.69	8.88	0.40	19.31	5.20	0.03	0.01	0	99.43	2	2
ROM263 GT52	41.97	0.98	20.52	1.01	8.95	0.23	20.52	4.42	0.09	0.00	0.0015	98.69	4	4
ROM263 GT25	41.85	1.14	21.15	0.77	9.90	0.25	19.83	4.60	0.10	0.00	0.0032	99.59	4	4
ROM263 GT09	41.53	1.17	21.18	0.57	10.85	0.27	19.21	4.54	0.10	0.00	0.0040	99.43	4	4
Dora Maira	43.52	0.02	25.60	0.01	0.89	0.02	29.31	0.06	0.02	0.02	0.0043	99.46	2	2
MON9GT	42.20	1.25	20.39	0.62	10.89	0.28	19.52	4.62	0.11	0.00	0.0056	99.89	6	6
Ant Hill Clear	39.45	0.02	23.30	0.04	18.43	0.37	10.93	7.84	0.02	0.02	0.0060	100.42	2	2
Ant Hill Dark	41.15	0.20	22.06	2.85	9.43	0.46	19.18	5.02	0.04	0.03	0.0189	100.43	2	2

Notes: References: 1 = Bryan and Moore (1977); 2 = This study; 3 = Withers and Behrens (1999); 4 = Bell et al. (2004); 5 = Koga et al. (2003); 6 = Bell et al. (1995); 7 = Fine and Stolper (1985/1986).

† FeO*: all Fe as Fe^{2+}.

TABLE 3. Infrared and SIMS data for the standards

Sample	Density ‖ (g/l)	H_2O (wt%) (glass or mineral-specific calibration)	H_2O (wt%) (Libowitzky and Rossman calibration)	Ref. H_2O §	^1H count (cps)	^{30}Si count (cps)	$^1H/^{30}Si$ (measured)	$^1H/^{30}Si$ (blank corrected) *
Basaltic glasses								
ALV519-4-1	2810	0.17 ± 0.01		1	1.41×10^{4}	9.40×10^{4}	1.50×10^{-1}	
JdFD10	2806	0.348 ± 0.021		2	2.16×10^{4}	9.57×10^{4}	2.26×10^{-1}	
KN54Sta52	2803	0.495 ± 0.034		2	4.22×10^{4}	8.67×10^{4}	4.87×10^{-1}	
KN54Sta51	2800	0.647 ± 0.029		2	4.26×10^{4}	8.90×10^{4}	4.78×10^{-1}	
AC49	2774	1.98 ± 0.05		2	9.52×10^{4}	7.76×10^{4}	1.23×10^{0}	
AC46	2735	3.91 ± 0.05		2	1.55×10^{5}	7.33×10^{4}	2.12×10^{0}	
AC47	2693	6.03 ± 0.05		2	2.08×10^{5}	6.69×10^{4}	3.11×10^{0}	
AC50	2661	7.65 ± 0.05		2	2.05×10^{5}	5.86×10^{4}	3.49×10^{0}	
Rhyolitic glasses								
Red Hill Cinder Cone	2388	0.14 ± 0.01		2	6.93×10^{3}	7.42×10^{4}	9.35×10^{-2}	
EDF natural	2386	0.23 ± 0.01		3	9.41×10^{3}	7.38×10^{4}	1.27×10^{-1}	
EDF1(E)	2349	0.97 ± 0.05		3	2.69×10^{4}	7.03×10^{4}	3.83×10^{-1}	
EDF1(H)	2339	1.68 ± 0.05		3	4.32×10^{4}	6.96×10^{4}	6.21×10^{-1}	
EDF2	2345	2.12 ± 0.05		3	3.32×10^{4}	6.66×10^{4}	4.99×10^{-1}	
EDF2.4	2342	2.74 ± 0.05		3	4.73×10^{4}	6.62×10^{4}	7.15×10^{-1}	
EDF3	2329	3.42 ± 0.05		3	8.50×10^{4}	6.55×10^{4}	1.30×10^{0}	
EDF4	2321	4.10 ± 0.05		3	8.92×10^{4}	6.39×10^{4}	1.40×10^{0}	
EDF4b	2321	4.20 ± 0.05		3	9.65×10^{4}	6.35×10^{4}	1.52×10^{0}	
EDF5	2299	5.16 ± 0.05		3	9.11×10^{4}	6.16×10^{4}	1.48×10^{0}	
EDF6	2284	6.20 ± 0.05		3	1.02×10^{5}	6.03×10^{4}	1.69×10^{0}	
Olivine crystals								
ROM177	3450	0.0125 ± 0.0013		4	7.66×10^{2}	7.13×10^{4}	1.07×10^{-2}	8.81×10^{-3}
ROM250 OL2	3408	0.0183 ± 0.0018		4	9.49×10^{2}	8.44×10^{4}	1.13×10^{-2}	9.61×10^{-3}
ROM250 OL13	3469	0.0243 ± 0.0024		4	1.72×10^{3}	8.80×10^{4}	1.96×10^{-2}	1.80×10^{-2}
AC90 rim †	3322	0.0079 ± 0.0008	0.0032 ± 0.0008	2	1.34×10^{3}	6.77×10^{4}	1.97×10^{-2}	1.77×10^{-2}
AC93 rim †	3333	0.0068 ± 0.0007	0.0028 ± 0.0007	2	1.03×10^{3}	1.40×10^{-2}	7.34×10^{4}	1.22×10^{-2}
AC86 rim	3311	0.0073 ± 0.0007	0.0023 ± 0.0006	2	1.91×10^{3}	7.60×10^{4}	2.52×10^{-2}	2.33×10^{-2}
Fo100	3226	0.0000 ± 0.0000	0.0000 ± 0.0000	5	7.80×10^{1}	1.07×10^{5}	7.29×10^{-4}	0.00×10^{0}
Damaping OL	3340	0.0001 ± 0.0001	<0.0001	2	1.35×10^{2}	1.36×10^{5}	9.93×10^{-4}	4.19×10^{-4}
Ant Hill OL	3322	0.0009 ± 0.0001	0.0004 ± 0.0001	2	2.65×10^{2}	1.29×10^{5}	2.05×10^{-3}	1.45×10^{-3}
San Carlos OL	3337	0.0001 ± 0.0001	<0.0001	2	7.97×10^{1}	7.56×10^{4}	1.05×10^{-3}	4.77×10^{-4}
AC56 core	3328	0.0064 ± 0.0006	0.0024 ± 0.0006	2	6.01×10^{2}	8.30×10^{4}	7.24×10^{-3}	5.58×10^{-3}
AC58 core	3335	0.0048 ± 0.0005	0.0022 ± 0.0006	2	5.48×10^{2}	7.44×10^{4}	7.37×10^{-3}	5.51×10^{-3}
AC84 core †	3343	0.0052 ± 0.0005	0.0023 ± 0.0006	2	5.24×10^{2}	7.18×10^{4}	7.30×10^{-3}	5.38×10^{-3}
AC85 core †	3345	0.0084 ± 0.0006	0.0036 ± 0.0009	2	9.66×10^{2}	8.38×10^{4}	1.15×10^{-2}	9.88×10^{-3}
AC89 rim ‡	3270	0.0271 ± 0.0030	0.0162 ± 0.0041	2	4.88×10^{3}	1.26×10^{5}	3.88×10^{-2}	3.81×10^{-2}
AC87 rim ‡	3342	0.0478 ± 0.0048	0.0281 ± 0.0070	2	4.43×10^{3}	7.81×10^{4}	5.67×10^{-2}	5.50×10^{-2}
AC94 rim	3337	0.0910 ± 0.0090	0.0635 ± 0.0159	2	1.86×10^{4}	1.19×10^{5}	1.56×10^{-1}	1.55×10^{-1}
Orthopyroxene crystals								
Bamble Dry	3297	0.0000 ± 0.0000	0.0000 ± 0.0000	2	6.23×10^{1}	8.59×10^{4}	7.25×10^{-4}	0.00×10^{0}
San Carlos OPX	3284	0.0038 ± 0.0004	0.0039 ± 0.0010	2	2.89×10^{2}	8.39×10^{4}	3.44×10^{-3}	2.92×10^{-3}
Bamble	3279	0.0055 ± 0.0006	0.0059 ± 0.0015	2	3.94×10^{2}	8.15×10^{4}	4.83×10^{-3}	4.30×10^{-3}
Damaping OPX	3308	0.0078 ± 0.0008	0.0091 ± 0.0023	2	5.57×10^{2}	8.15×10^{4}	6.83×10^{-3}	6.30×10^{-3}
India	3368	0.0141 ± 0.0014	0.0138 ± 0.0035	2	9.47×10^{2}	9.06×10^{4}	1.04×10^{-2}	9.97×10^{-3}
Kenya	3308	0.0147 ± 0.0015	0.0169 ± 0.0042	2	8.27×10^{2}	7.90×10^{4}	1.05×10^{-2}	9.92×10^{-3}
ROM167	3348	0.0215 ± 0.0022		4	1.54×10^{3}	9.05×10^{4}	1.70×10^{-2}	1.66×10^{-2}
KBH-1	3306	0.0217 ± 0.0022		6	1.47×10^{3}	7.99×10^{4}	1.84×10^{-2}	1.79×10^{-2}
ROM273-OG2	3308	0.0263 ± 0.0026		4	1.90×10^{3}	8.86×10^{4}	2.14×10^{-2}	2.09×10^{-2}
Clinopyroxene crystals								
PMR53HT	3314	0.0000 ± 0.0000		6	7.81×10^{1}	9.44×10^{4}	8.28×10^{-4}	0.00×10^{0}
Dish Hill	3403	0.0000 ± 0.0000	0.0000 ± 0.0000	2	6.68×10^{1}	9.19×10^{4}	7.26×10^{-4}	0.00×10^{0}
Damaping CPX	3312	0.0178 ± 0.0018	0.0147 ± 0.0037	2	7.93×10^{2}	8.20×10^{4}	9.67×10^{-3}	9.14×10^{-3}
Tungunska	3281	0.0106 ± 0.0011	0.0098 ± 0.0025	2	1.02×10^{3}	8.80×10^{4}	1.15×10^{-2}	1.10×10^{-2}
ROM271 DI10	3316	0.0195 ± 0.0020		4	7.64×10^{2}	9.29×10^{4}	8.23×10^{-3}	7.76×10^{-3}
PMR53	3314	0.0268 ± 0.0027		6	1.81×10^{3}	9.32×10^{4}	1.95×10^{-2}	1.90×10^{-2}
ROM271 DI16	3320	0.0439 ± 0.0044		4	2.21×10^{3}	9.06×10^{4}	2.44×10^{-2}	2.39×10^{-2}
ROM271 DI21	3336	0.0490 ± 0.0049		4	1.86×10^{3}	8.77×10^{4}	2.12×10^{-2}	2.07×10^{-2}
Garnet crystals								
Ant Hill Dry	3714	0.0000 ± 0.0000	0.0000 ± 0.0000	2	5.93×10^{1}	7.79×10^{4}	7.61×10^{-4}	0.00×10^{0}
ROM263 GT52	3712	0.0015 ± 0.0002		4	8.58×10^{1}	7.49×10^{4}	1.14×10^{-3}	5.61×10^{-4}
ROM263 GT25	3725	0.0032 ± 0.0003		4	1.82×10^{2}	8.27×10^{4}	2.20×10^{-3}	1.67×10^{-3}
ROM263 GT09	3740	0.0040 ± 0.0004		4	2.52×10^{2}	8.38×10^{4}	3.01×10^{-3}	2.49×10^{-3}
Dora Maira	3594	0.0044 ± 0.0004	0.0030 ± 0.0008	2	1.48×10^{2}	6.09×10^{4}	2.43×10^{-3}	1.71×10^{-3}
MON9GT	3738	0.0056 ± 0.0006		6	2.09×10^{2}	8.11×10^{4}	2.58×10^{-3}	2.04×10^{-3}
Ant Hill Clear	3866	0.0057 ± 0.0006	0.0032 ± 0.0008	2	2.45×10^{2}	7.52×10^{4}	3.26×10^{-3}	2.68×10^{-3}
Ant Hill Dark	3722	0.0189 ± 0.0019	0.0086 ± 0.0022	2	3.69×10^{2}	4.97×10^{4}	7.43×10^{-3}	6.55×10^{-3}

* The $^1H/^{30}Si$ blank-corrected ratios were calculated by subtracting the ^1H count of the blank from that of the sample and dividing the result by the observed ^{30}Si count of the sample.

† For samples AC84, AC85, AC90, and AC93, the reported H_2O concentration are determined from unpolarized FTIR measurements on randomly oriented grains with the Paterson (1982) calibration. An orientation factor of 1/3 has been used and the resulting concentrations have been increased by a factor of 3.5 to remain consistent with the measurements made with the calibration of Bell et al. (2003).

‡ For samples AC89 and AC94, the total water concentration is based on two directions only, the concentration on the third direction is estimated from the proportions of OH absorption along the three directions observed for the olivine AC87: $\alpha = 27\%$, $\beta = 16\%$, and $\gamma = 57\%$.

§References: 1 = Fine and Stolper (1985/1986); 2 = This study; 3 = Withers and Behrens (1999); 4 = Bell et al. (2004); 5 = Koga et al. (2003); 6 = Bell et al. (1995).

‖ Densities of basalts calculated from the relationship given by Yamashita et al. (1997). Densities of rhyolites are from measurements reported by Withers and Behrens (1999). For olivines, pyroxenes and garnets, the densities are calculated from the models of Fisher and Medaris (1969), Sack and Ghiorso (1994) and Berman and Koziol (1991), respectively.

Table 4. Major element of the starting materials used in the present study

	AC74	AC no. 2	San Carlos	Mix1-opx	Mix2-ol	Mix2-opx	Mix3-FP
n	20	10	10	10	4	5	6
SiO_2	50.05(0.55)	48.28(0.33)	40.34(0.30)	57.82(0.53)	41.55(0.27)	56.32(0.45)	0.22(0.51)
TiO_2	1.56(0.07)	0.46(0.04)	0.01(0.02)	0.02(0.03)	0.00(0.01)	0.05(0.02)	0.01(0.02)
Al_2O_3	15.94(0.19)	14.59(0.10)	0.01(0.01)	0.07(0.06)	0.07(0.07)	4.36(0.13)	0.00(0.01)
FeO	9.33(0.14)	7.95(0.15)	9.22(0.11)	9.66(0.51)	8.91(0.12)	5.62(0.09)	52.70(0.53)
MgO	8.35(0.12)	18.01(0.12)	49.52(0.23)	33.40(0.51)	49.76(0.14)	33.73(0.09)	46.91(0.40)
CaO	10.52(0.12)	9.00(0.19)	0.08(0.02)	0.22(0.08)	0.12(0.01)	0.73(0.03)	0.01(0.02)
Na_2O	3.00(0.11)	1.56(0.07)	0.01(0.01)	0.07(0.03)	0.02(0.01)	0.14(0.02)	0.05(0.03)
K_2O	0.21(0.03)	0.07(0.01)	0.02(0.01)	0.03(0.02)	0.01(0.01)	0.03(0.01)	0.03(0.02)
MnO	0.15(0.03)	n.d.	0.12(0.03)	0.06(0.02)	0.15(0.01)	0.13(0.02)	0.02(0.03)
Cr_2O_3	0.03(0.03)	n.d.	n.d.	n.d.	n.d.	n.d.	n.d.
NiO	n.d.	n.d.	0.38(0.04)	0.03(0.03)	0.25(0.07)	0.07(0.03)	0.05(0.04)
Total	99.14(0.62)	99.92(0.51)	99.68(0.44)	101.40(0.61)	100.80(0.39)	101.2(0.61)	100.00(0.57)

High-water content basaltic and rhyolitic glasses

For basaltic glasses with high water contents (>1 wt% H_2O), spectra were obtained with a Digilab Excalibur 4000 series infrared spectrometer equipped with a UMA600 microscope at University of Wisconsin, Eau Claire, using 1024 scans, a spectral resolution of 2 cm^{-1} and an aperture diameter of 100 μm. The light source, beamsplitter, and detector were tungsten/halogen, CaF_2, and liquid nitrogen cooled InSb, respectively.

For concentration measurements, we use the calibration of Ohlhorst et al. (2001) with a linear (TT) subtraction method and peak height measurement for the combination bands with absorption band maxima at ~5200 and ~4500 cm^{-1}. The 4500 cm^{-1} band is assigned to the combination of stretching and bending mode of structurally bonded OH and the 5200 cm^{-1} band to the combination of stretching and bending mode of H_2O molecules (H_2O_m) (Stolper 1982). Following Ohlhorst et al. (2001), baselines were chosen between 4280 and 4680 cm^{-1} for the 4500 cm^{-1} band and between 4680 and 5370 cm^{-1} for the 5200 cm^{-1} peak. Uncertainty in peak positions is ±2 cm^{-1} and errors in peak heights are ±0.003 absorbance units for the 4500 cm^{-1} OH peak and ±0.002 for the 5200 cm^{-1} H_2O_m peak. Basalt densities were calculated from the relation $\rho = -19.9\,C_{H_2O} + 2813$, where C_{H_2O} is total H_2O in wt%, as derived from the data of Yamashita et al. (1997) for basaltic glasses synthesized at 1.1–1.2 GPa. Since the total water content in this equation is not known a priori, the equation was combined with the Beer-Lambert law and the total water content was calculated iteratively. The high water content rhyolitic glasses were synthesized and analyzed by FTIR by Withers and Behrens (1999) (Table 3).

Low water content glasses and crystals

For low water content glasses and crystals, we used the Nicolet Series II Magna-IR 750 spectrometer equipped with a Nic-Plan microscope at University of Minnesota, an Ever-Glo (Globar) source, a Ge on KBr beamsplitter and a liquid nitrogen cooled MCT-A detector. For polarized infrared spectroscopy, a 1200 line/mm Zinc Selenide wire grid polarizer was used. Spectra were acquired with a 100 μm aperture, a resolution of 4 cm^{-1} and the number of scans varied from 128 to 2048, depending on the sample.

For low water content basalt glasses, we employed the calibration of Jendrzejewski et al. (1996), using a linear background subtraction method between ~2520 and ~3710 cm^{-1} and peak height measurement for the absorption band at 3540 cm^{-1}, treating the spectra with the algorithm developed by Agrinier and Jendrzejewski (2000). Uncertainties in the resulting water contents are about 60 ppm H_2O (Agrinier and Jendrzejewski 2000). The low water content rhyolitic glass was measured with the calibration of Dobson et al. (1989) with a linear background subtraction taken between 2520 and 3770 cm^{-1} and the total water measured from the peak at 3570 cm^{-1}.

For olivine, we applied the calibration of Bell et al. (2003) and for orthopyroxene, clinopyroxene and garnet we used those of Bell et al. (1995). These calibrations entail integration of absorbance bands in the region of OH stretching mode. For olivine, orthopyroxene, and clinopyroxene, the area corresponds to the sum of the areas along the three (α, β, γ) axes of the indicatrix. For garnet, the area is determined from unpolarized infrared spectra. In a few cases, olivines were measured by unpolarized FTIR. The H_2O content was determined with the calibration of Paterson (1982) with an orientation factor of 1/3. The resulting concentrations were increased by a factor of 3.5 to remain consistent with the calibration of Bell et al. (2003). An unpolarized measurement can result in results less accurate than when a polarized beam is use. This has been taken into account to calculate the uncertainties of the H_2O contents.

A key factor in the quantitative determination of H_2O content in nominally anhydrous minerals is the choice of baseline. For minerals, we use a third degree polynomial fit of spectra beneath the OH absorption peaks and these vary as a function of crystal type, axis and total water content. The appropriateness of the chosen baseline is always checked by observation. The baseline was subtracted from the raw spectrum and the OH absorption band area was calculated by integration. Baseline correction is thought to contribute the greatest uncertainty to absorption integrations, yielding an uncertainty that is believed to be ±10%. This uncertainty likely increases as total water content decreases.

Table 5. Run conditions for the synthesis of the high water content basaltic glasses

Sample	Capsule	*P* (GPa)	*T* (°C)	*t* (h)	H_2O wt%
AC74	Graphite	1	1600	0.5	0
AC46	$Au_{75}Pd_{25}$	1	1350	0.5	3.39
AC47	$Au_{75}Pd_{25}$	1	1300	0.5	4.85
AC49	$Au_{75}Pd_{25}$	1	1350	0.5	1.89
AC50	$Au_{75}Pd_{25}$	1	1300	0.5	7.69

Secondary ion mass spectrometry

Secondary ion mass spectrometry (SIMS) measurements of H in the samples were performed with the Cameca IMS 6f ion microprobe at Arizona State University (ASU).

Minimization of hydrogen background in the ion microprobe

The greatest challenge to measuring extremely low hydrogen concentrations using SIMS is minimization of the hydrogen background during analysis (Hauri et al. 2002; Koga et al. 2003). Under high or ultra-high vacuum (UHV), H_2O vapor and H_2 are the major gaseous components contributing to the hydrogen background. To diminish the partial pressure of these, we have established the following protocols in the ASU GeoSIMS laboratory. Many of these techniques are inspired by procedures pioneered by Erik Hauri at the Carnegie Institution (Hauri et al. 2002; Koga et al. 2003).

Sample preparation

We use an epoxy-free sample mounting technique similar to that developed by Hauri et al. (2002) and Koga et al. (2003). The samples are cut with a wire saw, mounted with Crystalbond 509 (Aremco Products) resin and polished with diamond lapping films as described above. Crystal bond is dissolved in acetone and then the samples are cleaned in acetone using a sequence of three baths of 20 min each, followed by three 20 min baths of ethyl alcohol and storage in a vacuum oven at 120 °C for at least 12 h. At this temperature, no significant diffusive loss of hydrogen occurs during storage.

Samples are mounted in aluminum disks as illustrated in Figure 1. The disks are placed on a hot plate at a temperature above 160 °C. The hole is filled with 1 mm indium spheres (Alfa Aesar Indium shot no. 40338). The spheres melt, owing to the low melting temperature of indium (~156 °C) and air bubbles are eliminated by stirring with a metal pick. The quantity of indium introduced in the disk should be slightly in excess of volume required to fill the hole, such that the surface of the indium protrudes slightly above the drilled hole. Then the disk is removed from the hot plate and allowed to cool to ambient temperature. Four holes are drilled through the bottom of the aluminum disk with a 1 mm diameter drill bit, as shown in Figure 1c. This permits the escape of excess indium as samples are pressed into the disk. The cleaned samples are pushed into indium by hand, using two superimposed glass slides and then, pressed in a 30 ton hydraulic press to achieve a flat surface on the

TABLE 6. Run conditions for the synthesis of the OH-bearing olivines

Run	Capsule	Starting material	Free H_2O	Powder	*P* (GPa)	*T* (C)	*t* (h)	H_2O present	Speciation
AC56	Au	San Carlos	Yes	Mix1-opx	3	1000	48	Yes	High=low
AC58	Au	San Carlos	Yes	Mix1-opx	2	1000	48	Yes	High=low
AC84	$Au_{75}Pd_{25}$	San Carlos	No	Brucite	2	1000	48	Lost	High=low
AC85	$Au_{75}Pd_{25}$	San Carlos	Yes	SCOL	3	1100	24	Yes	High=low
AC86	$Au_{75}Pd_{25}$	San Carlos	Yes	Mix2-ol+opx	3	1300	24	Yes	Low dominant
AC87	$Au_{75}Pd_{25}$	San Carlos	Yes	Mix3-FP	2	1300	24	Yes	High dominant
AC89	$Au_{75}Pd_{25}$	San Carlos	Yes	Mix3-FP	1.3	1300	24	Yes	High dominant
AC90	$Au_{75}Pd_{25}$	San Carlos	Yes	Mix2-ol+opx	1.3	1300	24	Yes	Low dominant
AC93	$Au_{75}Pd_{25}$	San Carlos	Yes	Mix2-ol+opx	2	1300	24	Yes	Low dominant
AC94	$Au_{75}Pd_{25}$	San Carlos	Yes	Mix3-FP	3	1300	24	Yes	High dominant

mount. Once all the samples are mounted onto the disk, gentle polishing with 1 μm alumina suspension is performed so that the free space between the edge of the sample and the indium is eliminated. The whole mount is then cleaned in three 20 min baths of acetone and three 20 min baths of ethyl alcohol and stored overnight in a vacuum oven at 50 °C. The mounts are coated with gold. To track hydrogen background variation and minimize inaccuracy from background differences among mounts, standards are mounted together with samples on each disk.

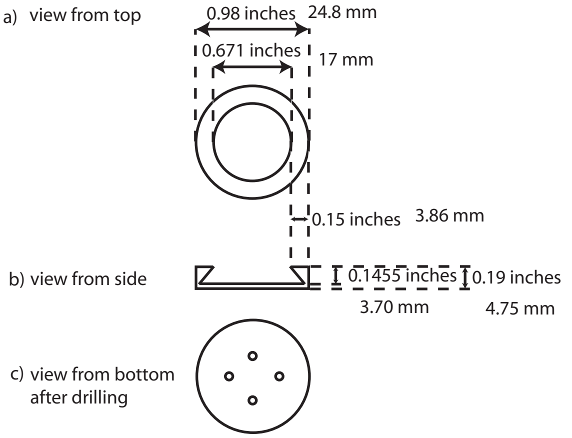

FIGURE 1. Schematic of the ion microprobe mount used to limit the hydrogen background. Units are presented both in inches and millimeters.

Ion microprobe baking and sample residence time under UHV

To achieve ultra high vacuum (UHV) in the sample chamber, the ion microprobe is baked for over 24 h before each analytical session. The pressure in the main sample chamber can be as low as ~2×10^{-10} Torr before and after sample introduction. When an epoxy-free sample mount is introduced into the main sample chamber the pressure in the sample chamber can normally decrease to <5×10^{-10} Torr in ~1–3 h when the liquid N_2 cold trap is used. However, our experience has shown that the hydrogen background at this stage is still too high for measuring low hydrogen concentrations. We have observed that under such UHV, the hydrogen on the sample surface cannot be "pumped" away directly as it can be under low vacuum. The decrease of hydrogen background or contamination on the sample surface can only be achieved by molecule collisions, which is a slow process under UHV. Thus, a very low ambient pressure in the sample chamber does not always guarantee a low hydrogen background in SIMS measurements. Most sample mounts need to stay under UHV for at least 24–48 h before low hydrogen analysis can begin. In practice, we always put the samples under UHV as early as possible, and while measuring the high hydrogen-content samples on one disk, one (or even more) sample disks are kept in the airlock section, which achieves a vacuum of 10^{-9} Torr when freshly baked.

Ion microprobe instrumental conditions

We optimized the configurations of the Cameca 6f ion microprobe for hydrogen analysis using the following conditions. We employ a 5–10 nA primary Cs^+ beam with impact energy of 19 KeV to sputter the samples. Using lower primary Cs^+ beam currents results in a dramatic diminishment in precision. The Cs^+ beam is tuned in aperture-illumination mode (Kohler illumination) to generate a uniform beam ~35 μm in diameter or tuned in critical illumination mode and rastered over a similar-sized area. Negative secondary ions were accelerated from the sample (held at –9 kV). By utilizing the smallest field aperture (100 μm), only ions originating from the central ~10 μm area of a crater were counted. Ions with excess kinetic energies of 0 ± 125 eV (energy bandpass centered and wide open) were allowed in the mass spectrometer, detected with an electron multiplier (EM), and corrected for background and for counting system deadtime. Each measurement runs 6 cycles through the mass sequence, ^{1}H, ^{12}C, ^{19}F, ^{30}Si, ^{32}S, and ^{35}Cl, with counting times of 5, 10, 5, 2, 5, and 5 seconds, respectively. The intensities of the ^{12}C, ^{19}F, ^{32}S, and ^{35}Cl signals have not quantified, but are monitored to allow identification of contaminants, such as glass inclusions or other foreign material in cracks, that might give inaccurate measurements of hydrogen in NAMs. Each analysis takes ~10 min, including 5 min rastering on a ~40 ×40 μm area to clean the analyzed area from surface-adsorbed contamination. The mass resolving power is set at 2500, sufficient to resolve ^{18}OH from ^{19}F and $^{16}O_2$ from ^{32}S. Sample charging is an important factor in SIMS measurements of non-conductive geological samples, and is compensated with an electron flooding gun. The electron gun is carefully tuned in two respects: (1) minimizing the electron current needed for charge compensation (<3 μA) so as to also minimize the yield of hydrogen ions generated by the electron beam and (2) adjusting the instrument so that all ions (from hydrogen to chlorine) are aligned on the ion optical axis. This is achieved by adjusting the electromagnets from electron steering (to achieve colinearity in y) and carefully placing an auxiliary permanent magnet between the transfer optics and electrostatic analyzer (for colinearity in x). This approach allows the operator to obtain the same ion ratios ($^{1}H^{-}/^{30}Si^{-}$) on the standards in analysis sessions several months apart.

RESULTS

Infrared spectroscopy

Basaltic and rhyolitic glasses. The infrared spectra in the wavenumber range 4000 to 6000 cm^{-1} of the four experimental basaltic glasses analyzed in the present study are shown in Figure 2a. Those of the experimental rhyolites are shown in Figure 2c. Their infrared spectra are typical of high water content glasses (Stolper 1982) and show both dissolved hydroxyl (4500 cm^{-1}) and molecular water (5200 cm^{-1}) bands. The infrared spectra between 2400 and 4000 cm^{-1} are shown in Figures 2b and 2d for the four natural low-water content basaltic and rhyolitic glasses analyzed in the present study. All of the samples show the typical OH stretching asymmetric absorption band with maximum intensity at 3570 cm^{-1} as previously reported for natural basaltic and rhyolitic glasses (e.g., Stolper 1982).

Olivine crystals. Previous work on natural and experimental olivines demonstrated that the infrared spectra for this mineral in the OH stretching region is extremely complex, with more than 40 infrared absorption bands identified so far (e.g., Bai and Kohlstedt 1992, 1993; Bell 1992; Bell et al. 2003; Beran and Putnis 1983; Berry et al. 2005; Freund and Oberheuser 1986; Khisina and Wirth 2002; Kitamura et al. 1987; Kohlstedt et al. 1996; Lemaire et al. 2004; Matsyuk and Langer 2004; Matveev et al. 2001; Miller et al. 1987; Zhao et al. 2004). In the pres-

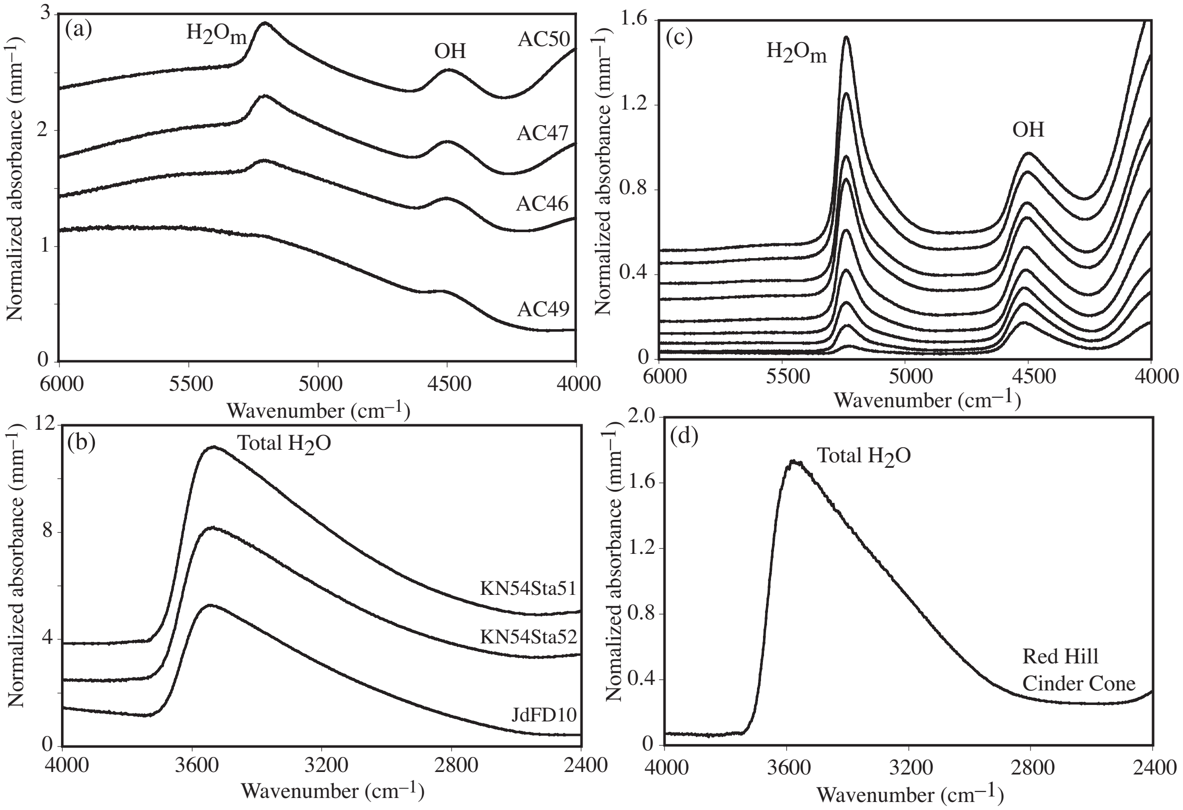

FIGURE 2. Unpolarized infrared spectra of (**a**) high-water content basaltic glasses (**b**) low-water content basaltic glasses (**c**) high-water content rhyolitic glasses (**d**) low-water content rhyolitic glass. All spectra are normalized to 1 mm thickness. Spectra are offset for clarity.

ent study, we obtained olivine crystals with a range of spectral characteristics (Fig. 3), allowing us to test whether olivine with different hydrogen substitutions produces distinct SIMS-FTIR calibration lines.

Natural olivines from spinel lherzolites. The three natural olivines from spinel lherzolites, from San Carlos, Arizona, Damaping, China, and the Navajo Nation, are relatively dry and contain less than 10 ppm H_2O (Table 3). Representative spectra for the Navajo Nation sample in 3 unique optical directions show the most commonly encountered OH absorption bands in olivine at 3612, 3598, 3572, 3525, 3480 cm^{-1}, which are most clearly resolved along the γ direction (Fig. 3b). Other peaks might be present but are difficult to resolve owing to the low hydrogen concentrations of these crystals. Olivines from San Carlos and from Damaping are nearly anhydrous, with H_2O below the ~1 wt. ppm detection limit of the FTIR technique.

Natural olivines from the Monastery kimberlite (South Africa). We analyzed three olivines (ROM177, ROM250-OL2, and ROM250-OL13) from the Monastery kimberlite. These samples were analyzed previously by FTIR by Bell et al. (2004), who noted numerous microscopic inclusions that likely account for some of the OH observed in the infrared absorption spectra. Most notably there is molecular water present in fluid inclusions and cracks and secondary hydrous phases, including serpentine. A representative set of spectra acquired during the present study (olivine ROM250-OL13) is shown in Figure 3f. Bell et al. (2004) previously reported FTIR spectra along the β and γ directions for the same crystals. Our results agree well with those of Bell et al. (2004) except that we observe a peak at 3250 cm^{-1} along the β direction that was not observed previously. This peak likely originates from a foreign phase included in the crystal. Several bands at wavenumbers above 3612 cm^{-1} are present, including 3670, 3637, and 3624 cm^{-1}, and these are generally attributed to serpentine, talc, and amphibole (Matsyuk and Langer 2004). The impact of these inclusions on the comparison between FTIR and SIMS analyses is considered below. When integrating the three directions, we obtain a total water concentration of 247 ppm in agreement with the multiple measurements made by Bell et al. (2004).

Olivines annealed at 1000–1100 °C. The olivines annealed at relatively low temperature (AC56, AC58, AC84, and AC85) show comparatively low hydrogen contents (between 50 and 100 ppm H_2O, Table 3). Infrared absorption spectra characteristic of these samples are shown in Figure 3c. These spectra have two groups of bands: (1) high wavenumber bands at 3612, 3598, 3572, and 3480 cm^{-1}, similar to the "group I" bands of Bai and Kohlstedt (1992, 1993) and (2) low wavenumber bands at 3386, 3356, 3329, and 3190 cm^{-1}, similar to the "group II" bands of Bai and Kohlstedt (1992, 1993). The pleochroic behavior of these bands, rarely documented in the literature, agrees well with the spectra reported in Bell et al. (2003) (their Fig. 4). High and low wavenumber OH absorption bands contribute approximately equally to the total H_2O concentration (Fig. 3c). One limitation of the IR quantitative measurements is that the molar absorp-

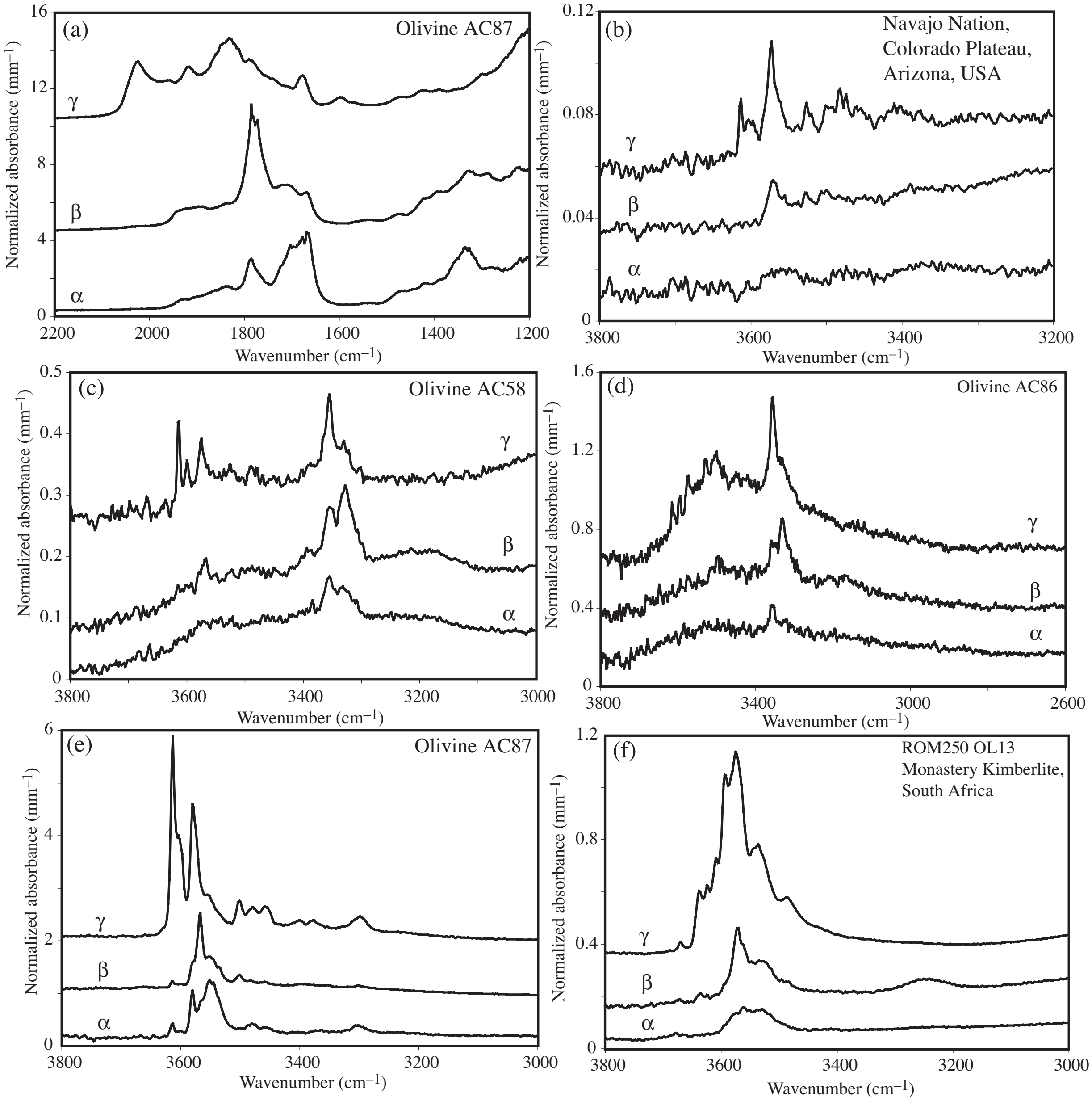

FIGURE 3. Representative polarized infrared spectra of natural and experimental olivines. (**a**) Polarized FTIR spectra of experimental olivine AC87 in the 1200–2200 cm^{-1} region showing the Si-O overtone absorption patterns used to identify the three principal axes [following Lemaire et al. (2004) and Asimow et al. (2006)]. (**b**) Polarized FTIR spectra of natural olivine from the Navajo Nation (Colorado Plateau, Arizona, U.S.A.). The total water concentration is 9 wt. ppm. (**c**) Polarized FTIR spectra of experimental olivine AC58 showing the two groups of absorption bands. Total water concentration is 48 wt. ppm. (**d**) Polarized FTIR spectra of experimental olivine AC86 showing predominantly the low wavenumber bands. The broad asymmetric absorption feature in the region 2800–3750 cm^{-1} probably corresponds to inclusions of a hydrous phase. (**e**) Polarized FTIR spectra of experimental olivine AC87 in the 3000–3800 cm^{-1} region showing predominantly the high wavenumber bands. The total water content of the olivine is 480 wt. ppm H_2O. (**f**) Polarized FTIR spectra of the natural olivine ROM250 OL13 from the Monastery Kimberlite (South Africa). The concentration reported by Bell et al. (2004) is 243 wt. ppm H_2O. The present calibration work suggests that the actual concentration of dissolved hydrogen in the crystal is 113 wt. ppm. Overestimation of the concentration by Bell et al. (2004) is probably due to the presence of foreign phases as suggested by the peaks at 3670, 3637, 3624 cm^{-1}. All spectra are normalized to 1 mm thickness. Spectra are offset for clarity.

tivity, ε established by Bell et al. (2003) is applicable only to high wavenumber OH absorption (group I) bands. Based on the variation of ε values with wavenumber observed by Libowitzky and Rossman (1997), Bell et al. (2003) suggested that the ε value that should be applied to the group II bands is possibly a factor 2 higher that that determined for the group I bands. However, it is not known whether a simple relationship between molar absorptivity and wavenumber can be applied to NAMs, although

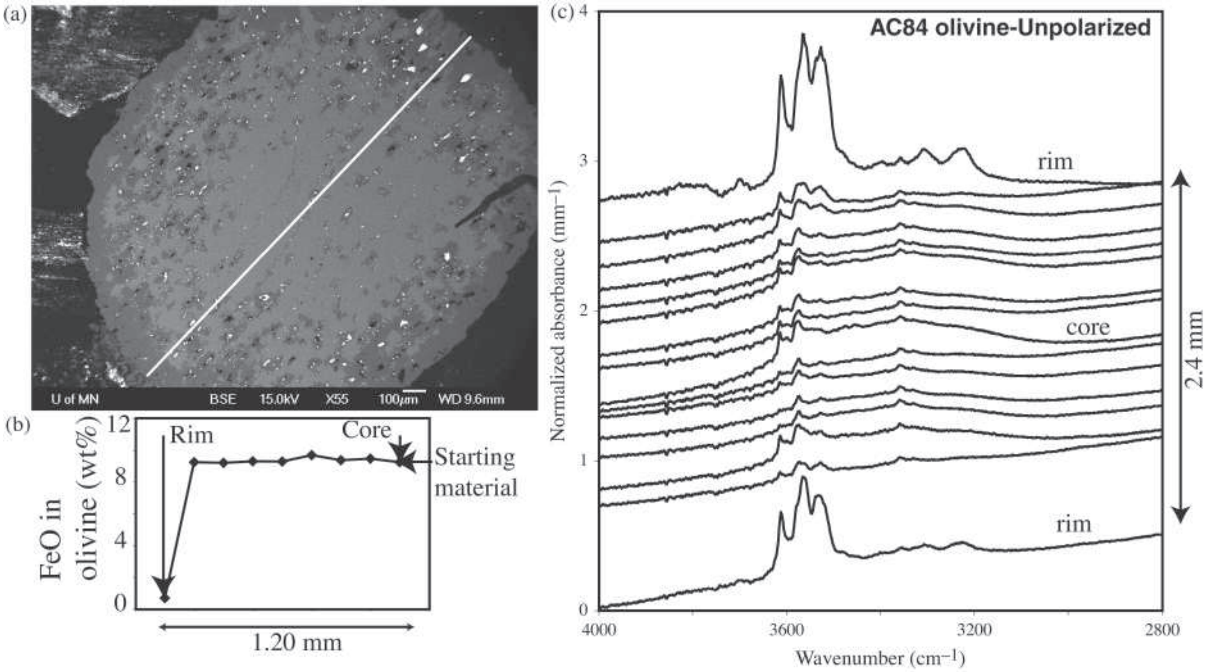

FIGURE 4. Olivine AC84 after annealing and polishing. The olivine was put into the capsule as a rounded single crystal and remained intact throughout the experiment and quench process. (**a**) Back-scattered electron image of the olivine AC84. The darker 100 μm rim and the small dark patches inside the olivine have a Fo98.5 composition resulting from dissolution-reprecipitation processes while the light gray area has the composition of the starting material (Fo90). The size of the olivine along its longest direction (as indicated by the white line) is 2.4 mm. (**b**) FeO* (all iron as Fe^{2+}) content semi-profile (from rim to core) of the experimental olivine AC84 showing that the rim evolved to a composition of Fo98.5. (**c**) Unpolarized FTIR spectra of a profile measured from rim to rim along the longest direction of the olivine AC84 (see white line on **a**). The relatively high absorption observed at the forsterite-rich rim suggests much higher water contents in the rim than inside the olivine. The starting material was almost dry with no discernable absorption in the OH stretching region. All spectra are normalized to 1 mm thickness. Spectra are offset for clarity.

such relationships have been demonstrated to be useful for stoichiometric OH-bearing minerals and glasses (Libowitzky and Rossman 1997; Paterson 1982). Moreover, coupled SIMS and unpolarized IR analyses from Koga et al. (2003) indicate that the ε value determined by Bell et al. (2003) may be applicable to the low wavenumber OH absorption bands without introducing significant bias to the inferred H_2O concentrations. We therefore apply the ε value determined by Bell et al. (2003) to the entire OH absorption spectra observed in these crystals and then discuss potential differences between SIMS-FTIR comparison for the different types of olivines.

The majority of the olivine grains annealed at 1000–1100 °C preserve the major element composition of the starting material and are homogeneous in OH content. In only one case (AC84), the olivine rim has much higher water than its core, as illustrated in Figure 4. This olivine, annealed in the presence of brucite powder, has undergone some Fe-Mg exchange with the surrounding powder and developed a forsterite-rich rim (see the darker rim in the backscattered electron image shown in Fig. 4a and the rim to core FeO profile in Fig. 4b). Fe–Mg exchange probably through solution-precipitation processes also occurred inside the olivine along cracks and dissolution channels developed during the hydrothermal experiments. The hydrogen content of the core (52 wt. ppm) is much higher than that of the starting material (natural San Carlos olivine with less than 1 wt. ppm H_2O). The most straightforward explanation is that relatively rapid diffusion of hydrogen allows decoration of the existing defects of the olivine starting crystal with OH but more sluggish Fe-Mg and Si diffusion did not allow complete equilibration of the core of the olivine with its chemical environment. For the crystal rim, Fe-Mg equilibration was more nearly approached, and the same may or may not have been true with respect to silica activity (and hence, for tetrahedral and octahedral vacancies and substitutions). Nevertheless, the defect populations of the rim and core clearly differ as reflected in the different water contents and IR peaks. For this sample, we compare SIMS and polarized FTIR only for the core of the crystal.

Olivines annealed at 1300 °C in the presence of orthopyroxene. Three olivines were annealed in the presence of orthopyroxene (AC86, AC90, AC93). The rims of these olivines show mainly the low wavenumber OH absorption bands (group II bands), consistent with the results of Matveev et al. (2001). Representative spectra of these olivines are shown in Figure 3d (olivine AC86). These spectra also show a broad asymmetric absorption band with a maximum absorbance at 3500 cm^{-1}. Previously, this band has been attributed to molecular water in submicroscopic inclusions (Matveev et al. 2001). One surprising result of these measurements is that this broad asymmetric absorption band shows a pleochroic behavior (twice as much absorption along the γ direction than the α and β directions), which seems incompatible with inclusions of molecular water. This absorption band may be due either to hydroxyl bound in an anisotropic lattice of inclusions, or from molecular H_2O bonded to planar structure. In any case, as we consider this absorption to originate from a phase that is not dissolved in the crystal lattice, we do not integrate its contribution during assessment of the H_2O content. The run at 1.3 GPa produced large quantities of partial melt, which is not surprising as the system is above the wet solidus of harzburgite at these conditions (Parman and Grove 2004). Olivines produced at these conditions generally have less than 100 ppm H_2O (Table 3). Finally, we note that the ~2 mm olivine spheres introduced in the capsule did not fully equilibrate with the surrounding mineral+fluid buffer. Only the ~500 μm rims show evidence of major element and H_2O re-equilibration while the cores resemble those of the olivine annealed at lower temperature.

Olivines annealed at 1300 °C in the presence of ferropericlase. Three olivines were annealed in the presence of ferropericlase. The rim of these olivines show high water contents (Table 3) and exhibit mainly high wavenumber OH absorption bands (Fig. 3e), consistent with the experiments of Matveev et al. (2001). Once broad asymmetric absorption bands of the type described in the previous section are removed, 14 OH^- absorption peaks can be deconvoluted from these spectra at 3612, 3598, 3579, 3558, 3541, 3525, 3502, 3480, 3458, 3400, 3387, 3356, 3329, and 3300 cm^{-1}. These observations indicate that the hydrogen incorporation is enhanced by the relatively low silica activity conditions imposed by the olivine+ferropericlase buffer.

Despite relatively high annealing temperatures (1300 °C), the hydrogen distributions in the olivine crystals hydrated in the presence of ferropericlase are not completely homogeneous. For the 2 mm single crystals of olivine used as starting materials, only the ~500 μm rims have reached major element and hydrogen equilibrium with the thermochemical environment, as for the orthopyroxene buffered samples. The polarized FTIR and SIMS measurements reported in Table 3 have been made as close to the rim of the olivine crystal as possible.

Orthopyroxene crystals. Infrared spectra for orthopyroxene crystals are shown in Figure 5 and the quantitative H_2O concentrations are listed in Table 3. The orthopyroxene crystal from Bamble, Norway was dehydrated for three days (see above) to produce a completely dry crystal (Table 3). Other analyzed crystals show at least 7 absorption peaks with maximum peak height at 3600, 3570, 3520, 3410, 3300, 3210, and 3060 cm^{-1}, typical of aluminous orthopyroxene, (e.g., Peslier et al. 2002; Skogby et al. 1990; Stalder 2004). All analyzed orthopyroxenes show strongly pleochroic OH absorption with $\gamma > \alpha > \beta$ (Fig. 5) in agreement with the findings of Stalder (2004) for orthopyroxene with low (<200 ppm) total water contents.

In detail, orthopyroxene FTIR spectra vary from one crystal to another, possibly reflecting major element differences or different modes of incorporation in the crystal lattice. The infrared absorption spectra of the San Carlos (Fig. 5a) and Bamble (Fig. 5b) orthopyroxene are similar to those previously published for other natural orthopyroxenes (Peslier et al. 2002; Skogby et al. 1990). The spectrum for the Bamble orthopyroxene is quite different from that observed previously from crystals from this locality, in part because it lacks bands attributable to amphibole inclusions (Skogby et al. 1990). The spectrum of the orthopyroxene from India (Fig. 5c) differs from the Bamble and San Carlos crystals and shows strong similarities to spectra reported from Indian orthopyroxene by Skogby et al. (1990). The infrared spectra for the orthopyroxene from Kenya (Fig. 5d) bears strong similarities with the Simcoe orthopyroxene of Peslier et al. (2002) and the KBH-1 orthopyroxene of Bell et al. (1995).

The orthopyroxene from the Damaping spinel lherzolite (Fig. 5e) shows an additional peak with a maximum at 3680 cm^{-1} in the α-β plane. Because this absorption band is not usually present in orthopyroxene crystals (e.g., Peslier et al. 2002, this study; Skogby et al. 1990) and is not present in the β-γ plane, we infer that it originates from inclusions that are preferentially oriented in the crystal. Previously, it has been hypothesized that this band originates from amphibole lamellae (Skogby et al. 1990) with the strongest absorbance along the β direction and the weakest along the γ direction. For the Damaping orthopyroxene, subtraction of the spectra in the β direction showing no 3680 cm^{-1} band from the spectra in the β direction showing this band, (Fig. 5e) shows that the foreign phase contribution is strongly asymmetric and occurs over the broad region from 2900 to 3800 cm^{-1}. Previous work on FTIR spectra of amphiboles indicates the OH^- absorption region is typically sharp and narrow (e.g., Hawthorne et al. 2000; Ishida and Hawthorne 2001). This suggests that the foreign phase contribution isolated by our subtraction method is not only due to amphibole but to another phase, most likely water bound to planar cleavage surfaces, as previous experimental work has shown that both these hydrogen phases commonly develop together (Ingrin et al. 1989) and as the peak shape agrees with this interpretation. However, these different contributions are difficult to separate because of significant peak overlaps. To isolate the lattice bound H contribution and remove contamination from the combined effects of amphibole ± water bound to planar cleavage surface, we compared the spectra in the α-β and β-γ directions to determine the effect of the inclusions in the β direction. To correct the spectra in the α direction, we multiplied the β direction contamination peak (Fig. 5f) by an appropriate factor until the 3680 cm^{-1} peak in the α direction was eliminated. This procedure assumes that the shape of the foreign phase band is similar in the α and β directions. If this approximation is not accurate, it may contribute some uncertainty to the resulting corrected H_2O concentration measured along the α direction.

Clinopyroxene crystals. Infrared spectra for clinopyroxenes are presented in Figure 6 and H_2O determinations are listed in Table 3. The clinopyroxene from Dish Hill is completely OH^- free. The polarized infrared spectra of the Cr-diopside from Tungunska (Fig. 6a) are similar to those published by Bromiley et al. (2004). The infrared spectra show at least four absorption peaks at maximum peak heights of 3645, 3530, 3440, and 3350 cm^{-1}, in agreement with previous studies (e.g., Skogby et al. 1990). Deconvolution of the individual peaks suggests that at least one additional peak at around 3620 cm^{-1} is required to explain the shoulder observed on the 3645 cm^{-1} peak. The clinopyroxene from the Damaping lherzolite (Fig. 6b), like the orthopyroxene in the same rock, shows amphibole lamellae contributing to the spectra, though in the case of clinopyroxene, it is oriented in the β and γ plane. The same type of correction as that described above for the orthopyroxene has been made for

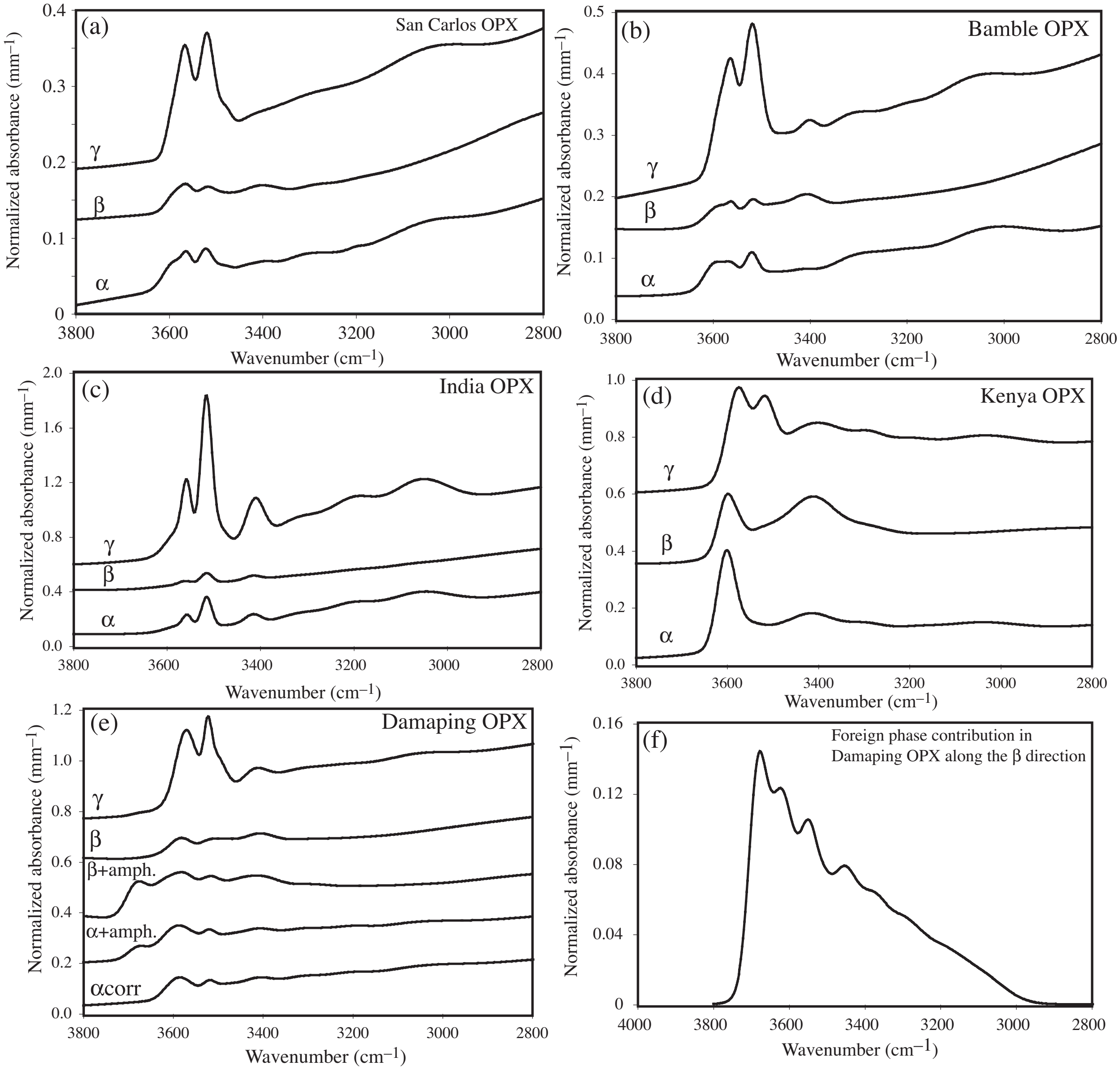

FIGURE 5. Polarized FTIR spectra of the orthopyroxenes analyzed in the present study. (**a**) Natural orthopyroxene from San Carlos with 38 wt. ppm H_2O. (**b**) Natural orthopyroxene from Bamble with 55 wt. ppm H_2O. (**c**) Natural orthopyroxene from India with 141 wt. ppm H_2O. (**d**) Natural orthopyroxene from Kenya with 147 wt. ppm H_2O. (**e**) Natural orthopyroxene from Damaping with 78 wt. ppm H_2O. Foreign phases absorb in the α-β plane. The α_{corr} spectrum was obtained by subtracting the foreign phase contribution (**f**) from the $\alpha_{+amph.}$ spectrum. (**f**) Foreign phase contribution obtained by subtracting the β spectrum from the β_{+amph} spectrum. All spectra are normalized to 1 mm thickness. Spectra are offset for clarity.

this crystal. The residual spectrum attributed to foreign phases along the γ direction is shown in Figure 6c. The persistence of sharp peaks within the portion of the spectrum attributed to lattice-bound H_2O suggests that the correction is not perfect, adding some uncertainty to the corrected H_2O concentration reported in Table 3. Like the orthopyroxene from Damaping, this crystal might not be ideal as a standard.

Garnet crystals. The Dora Maira pyrope used for the present study is colorless in mm thick sections. It shows four sharp peaks at 3602, 3641, 3651, and 3662 cm^{-1} in accordance with previous studies (Lu and Keppler 1997; Rossman et al. 1989) (Fig. 7). The peak height absorbance of the 3602 cm^{-1} peak is 0.28 abs mm^{-1}, similar to that (0.29 abs mm^{-1}) observed for pyrope by Rossman et al. (1989) and slightly lower than that (0.34 abs mm^{-1}) applied by Lu and Keppler (1997). It is not known if the absorption coefficient determined by Bell et al. (1995) is applicable to the Dora Maira pyrope because the infrared spectrum is different from those of common mantle-derived pyrope garnets, which likely reflects different sites for hydrogen incorporation in the crystal lattice. Comparison of our FTIR and SIMS observations of Dora Maira pyrope and other garnets allows us address this question. Note that weak absorption bands between 3500 and 3600 cm^{-1} may be caused by chlorite inclusions (see Blanchard and Ingrin 2004) but the contributions of these bands to the total water content is negligible.

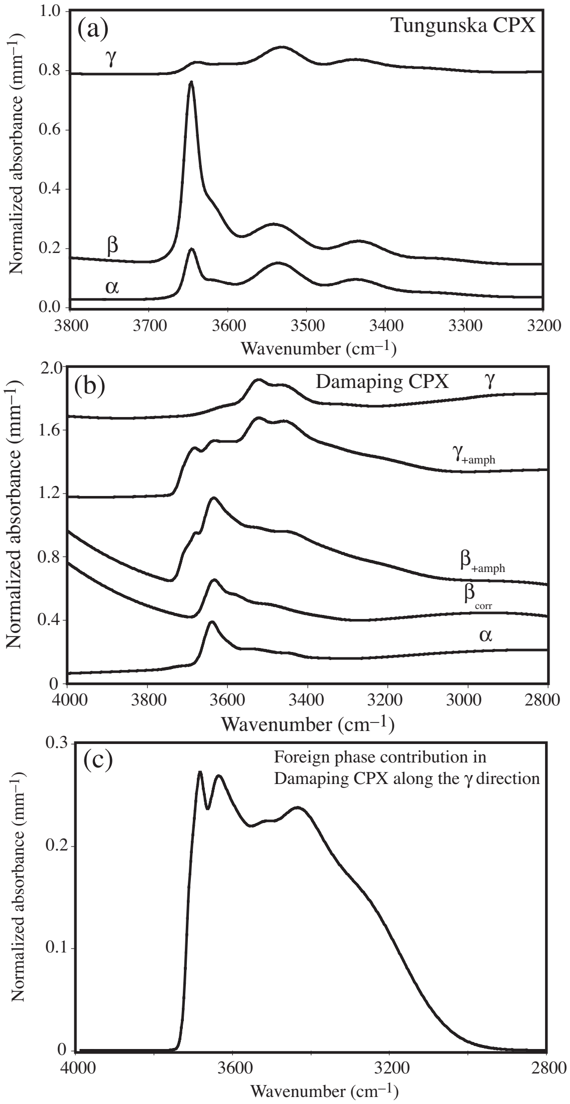

FIGURE 6. Polarized FTIR spectra of the clinopyroxenes analyzed in the present study. (**a**) natural clinopyroxene from Tungunska with 106 wt. ppm H_2O. (**b**) natural clinopyroxene from Damaping with 178 wt. ppm H_2O. Foreign phases absorb in the β-γ plane. The β_{corr} spectrum was obtained by subtracting the foreign phase contribution (Fig. 6c) from the β_{+amph} spectrum. (**c**) foreign phase contribution obtained by subtracting the γ spectrum from the γ_{+amph} spectrum. All spectra are normalized to 1 mm thickness. Spectra are offset for clarity.

The pyrope-rich garnet crystals from the Navajo Nation (Colorado Plateau, Arizona, U.S.A.) show three well-resolved absorptions bands with maxima at 3680, 3650, and 3570 cm^{-1} and possibly two other absorption bands with maxima at 3512 and 3450 cm^{-1} (Fig. 7). The infrared spectra of the Ant Hill Dark pyrope is similar to those previously observed for garnets with similar major element composition from diatremes of the Colorado Plateau (Aines and Rossman 1984; Wang et al. 1999, 1996). The dehydration experiment conducted on a 1.40 mm thick sample of Ant Hill garnet from the Navajo Nation (Colorado Plateau, Arizona, U.S.A.), resulted in a completely dry garnet with no observable OH^- peak (Fig. 7).

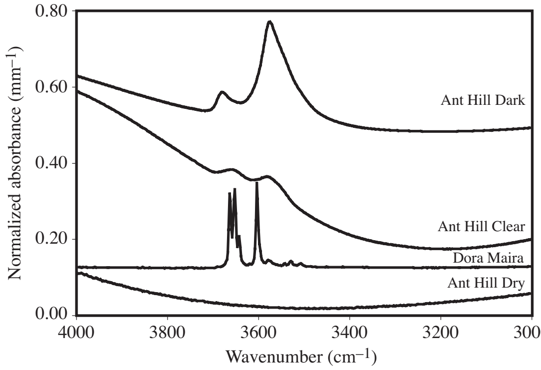

FIGURE 7. Unpolarized FTIR spectra of the garnets analyzed in the present study. All spectra are normalized to 1 mm thickness. Spectra are offset for clarity.

SIMS Calibration

The SIMS calibrations produced in the present study are shown in Figure 8. We chose to compare SIMS measurements using plots of H_2O measured in the standard by FTIR vs. $^{1}H/^{30}Si \times SiO_2$, where the latter derives from the product of $^{1}H/^{30}Si$ beam intensity ratio measured by SIMS and SiO_2 in wt%, measured by microprobe analysis. This representation allows visualization of the H_2O content of the samples whilst also facilitating comparison between standards with different concentrations of the normalizing element, which is a prerequisite for examining matrix effects on SIMS analyses of ^{1}H.

Estimation of hydrogen background in SIMS. The large number of nearly anhydrous standards (Table 1), including crystals with no detectable H_2O (2 olivines, 2 clinopyroxenes, 1 garnet and 1 orthopyroxene) and two olivine crystals with less than 1 wt. ppm H_2O, allows rigorous analysis of the H_2O background during typical analytical conditions. Seven of these 8 blank standards produce ^{1}H counting rates ranging from 59 and 80 cps, whilst the eighth, the Damaping olivine, yielded 135 cps. We conclude that in most cases the blank amounts to ~70 ± 10 cps and we use this value to calculate blank-corrected $^{1}H/^{30}Si$ in the rest of our standard minerals (Table 3). The olivine from the Navajo Nation, with 9 wt. ppm H_2O, produced 265 ^{1}H cps, illustrating that under typical operating conditions, the minimum detection limit is well below 9 wt. ppm. On the other hand, Monastery garnet ROM263 GT52, with 15 wt. ppm H_2Oproduced 86 ^{1}H cps, indicating that accurate analysis of samples with ~10–20 wt. ppm H_2O may be difficult when H background conditions are less than ideal.

Basalt and rhyolite calibrations. As shown in Figure 8a, there is a good proportionality between the water content determined by FTIR and the SIMS measurements with a slope of 0.0418 ± 0.0018 ($r^2 = 0.97$) for basalt glasses (in the following sections, we quote all the uncertainties in the zero-intercept slopes at the 95% confidence level). For high-water content basaltic glasses produced in experiments, the SIMS measurements were made in the center of the capsule in the same vicinity as the FTIR observations. SIMS analyses close to the walls of experimental capsules produced systematically lower $^{1}H/^{30}Si$ ratios, though the reason for this is not clear. Although we apply a linear fit to the calibration data, it is possible that the

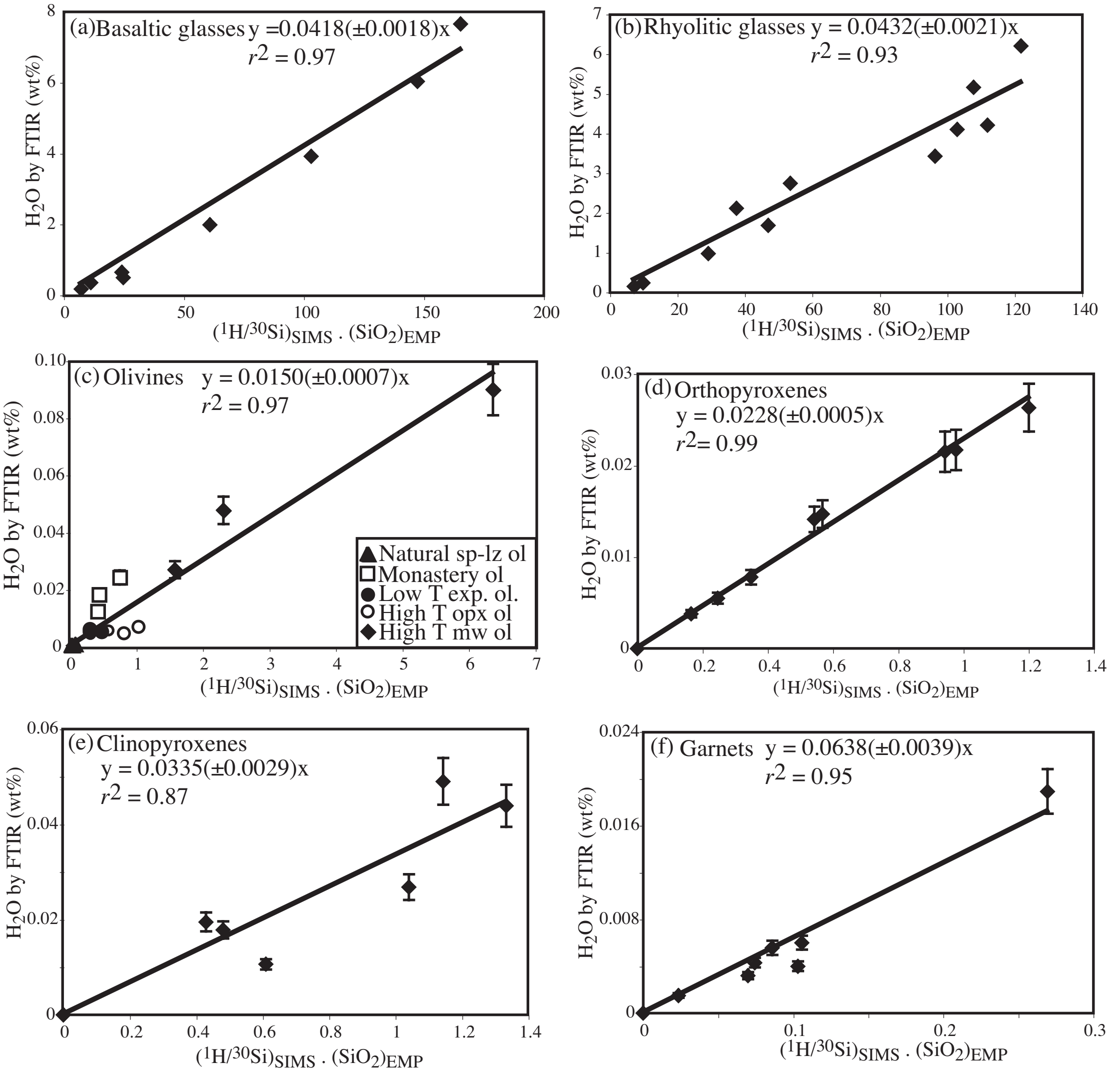

FIGURE 8. FTIR-SIMS calibration curves. (**a**) basaltic glasses, (**b**) rhyolitic glasses, (**c**) olivines, (**d**) orthopyroxenes, (**e**) clinopyroxenes, and (**f**) garnets. Quoted uncertainties on the zero-intercept slopes are at the 95% confidence level (2σ).

calibration departs from linearity at high H_2O contents (Fig. 8a) and that a quadratic calibration would be more appropriate. The FTIR and SIMS measurements of rhyolite glasses show a strong linear correlation with a slope of 0.0432 ± 0.0021 ($r^2 = 0.93$). The slopes of the basalt and rhyolite glass calibrations are not distinguishable from one another.

Olivine calibration. As shown in Figure 8c, natural olivines from spinel lherzolite, olivines annealed at 1000–1100 °C, and olivines annealed at 1300 °C in the presence of ferropericlase all plot along a single linear trend which yields a slope of 0.0150 ± 0.0007 and a correlation coefficient, r^2, of 0.97. However, the three olivines from the Monastery kimberlite, analyzed previously by Bell et al. (2004), plot significantly above the calibration curve, suggesting that the FTIR analyses represent greater H_2O than that evident from SIMS. As noted above, this probably means that the concentration of lattice-bound hydrogen in these olivines is overestimated by the FTIR analyses, perhaps owing to difficulties in resolving contributions from different hydrogen-bearing inclusions to the infrared spectra. Therefore, these samples have not been included in the regression of the calibration curve. Applying the calibration line defined by the samples described above, we obtain water concentrations of 63, 66 and 113 ppm H_2O in ROM177, ROM250-OL2, and ROM250-OL13, respectively, which are approximately half those reported by Bell et al. (2004) (Table 1). We infer that SIMS may be more effective than FTIR at determining lattice-bound OH^- for natural samples that have microscopic inclusions.

Two of the olivines (samples AC86 and AC90) annealed at relatively high temperature in the presence of orthopyroxene plot below the main calibration line (Fig. 8c). The reason for this observation is unclear but could be that (1) inclusions whose contribution was excluded from the FTIR measurement of H_2O concentration might also be sampled by the ion beam of the SIMS, or (2) application of the molar absorption coefficient from Bell et al. (2003) may not be appropriate as it was obtained only for the high wavenumber bands in the 3600–3450 cm^{-1}

domain. Therefore, these three samples have been excluded in the regression of the calibration curve.

Orthopyroxene calibration. Of all the NAMs, the calibration obtained for the orthopyroxenes (Fig. 8d) is the best defined, giving a slope of 0.0228 ± 0.0005 ($r^2 = 0.99$). Since it includes measurements from the study of Bell et al. (2004) as well as measurements performed by the present study, the calibration curve suggests that there is no systematic difference in H_2O concentration determination made at Minnesota as compared to that of Bell et al. (2004). This gives us confidence that the baseline subtractions used in the two infrared studies are comparable. The Damaping orthopyroxene that contains amphibole bands plots directly on the calibration line suggesting that (1) the amphibole inclusions are not sampled by the ion beam during SIMS measurements and (2) the correction applied to the infrared spectra to remove the contribution from these foreign phases is effective. We note that, contrary to the inferences of Koga et al. (2003), the SIMS calibration factor for orthopyroxenes is significantly different from that found for olivines.

Clinopyroxene calibration. The calibration curve for clinopyroxenes shows that there is a proportionality between FTIR and SIMS measurements with a slope of 0.0335 ± 0.0029 ($r^2 = 0.87$, Fig. 8e). However, the scatter is greater than for the orthopyroxenes. This could be due to variations in FTIR ε molar absorptivity values with complex clinopyroxene composition not taken into account in the study of Bell et al. (1995). The clinopyroxene from Damaping that shows some amphibole band contribution to its infrared spectrum does not deviate notably from the trend defined by the other samples. The slope of the calibration curve for clinopyroxene is significantly different from those of the olivines and the orthopyroxenes.

Garnet calibration. The garnet calibration (Fig. 8f) shows that there is a good proportionality between the FTIR and SIMS measurement for the garnet crystals, yielding a slope of 0.0638 ± 0.0039 ($r^2 = 0.95$). As previously observed by Koga et al. (2003), the slope is significantly larger than those of olivine, orthopyroxene, clinopyroxene, and basalt glass.

Rossman et al. (1989) showed that the pyropes from the Dora Maira massif have infrared spectra notably different from those of most of other mantle-derived pyrope-almandine garnets, raising concerns about the appropriateness of using the molar absorptivity determined by Bell et al. (1995). However, the Dora Maira pyrope plots on the same calibration line as the other garnets analyzed in this study, which suggests that the molar absorptivity determined by Bell et al. (1995) is applicable to this Dora Maira pyrope. From a theoretical point of view, this can be justified by the fact that both type of garnets show OH absorption features over a similar range of wavenumbers, as the IR molar absorptivity may depend chiefly on wavenumber rather than on the details of the spectrum (e.g., Libowitzky and Rossman 1997).

DISCUSSION

Matrix effects

A central question regarding SIMS analyses of H is the extent to which observed $^{1}H/^{30}Si$ beam intensity ratios are influenced by the composition of the matrix. In our observations, significant variations in major element composition among samples that are the same phase (intraphase variations) do not result in significantly different relationships between values of ($^{1}H/^{30}Si$) $\times$ (SiO_2) vs. H_2O observed by FTIR. This is true even for phases for which major element compositions vary significantly. For example, analyzed garnets range from 0.9 to 18.4 wt% FeO* (Table 2), but all plot along a single trend in Figure 8f. Similarly, the slopes observed for basaltic and rhyolitic glasses are indistinguishable (Figs. 8a and 8b).

As noted in the introduction, the magnitude of matrix effects for H analysis of SIMS has varied in different studies (Deloule et al. 1995; Hauri et al. 2002; Hinthorne and Andersen 1975; King et al. 2002; Sobolev and Chaussidon 1996), which is not surprising given the expected influence of different beam conditions (Ihinger et al. 1994). Consequently, the studies that may be most comparable to the present work are those of Hauri et al. (2002) and Koga et al. (2003), who also used a Cs^+ beam and counted negative ions with a Cameca 6f instrument. Although Hauri et al. (2002) and Koga et al. (2003) inferred significant matrix effects for analyses of silicate glasses and nominally anhydrous minerals, they did so by comparison of H_2O concentrations in standards with $^{1}H/^{30}Si$ beam intensities. Intraphase matrix effects from these studies are largely mitigated if the H_2O concentrations are compared to ($^{1}H/^{30}Si$) $\times$ (SiO_2).

Although our calibration shows little evidence for intraphase matrix effects, we do observe large apparent interphase matrix effects. Thus, single-phase calibration slopes vary by more than a factor of 4, from 0.015 for olivine to 0.064 for garnet. This variability is not due to differences in bulk compositional parameters such as mean atomic weight, SiO_2 concentrations, and FeO* concentrations between the different phases examined, because intraphase variations of these parameters for glasses and garnets are similar to or larger than interphase variations. Although we do not know the source of the observed interphase matrix effects, there are several possible explanations. Either these differences in slope reflect systematic difference in the phase-specific FTIR absorption calibration used to infer water concentrations in each phase or the behavior of each phase under the Cs^+ beam is affected by structural and/or bonding characteristics.

There has been considerable progress in developing phase specific FTIR calibrations against independent standards (Bell et al. 1995; Bell et al. 2003; Maldener et al. 2003), but the possibility remains that the phase-specific calibrations for nominally anhydrous minerals have significant inaccuracies. Nonetheless, FTIR absorption schemes for basaltic and rhyolitic glasses are probably reasonably accurate, given extensive efforts at intercalibrating FTIR with robust techniques such as manometry and Karl-Fischer titration (Dobson et al. 1989; Jendrzejewski et al. 1996; Ohlhorst et al. 2001), which provide accurate independent analyses for highly hydrous glasses. Thus, if interphase SIMS/FTIR calibration discrepancies are owing to problems with phase specific FTIR absorption schemes, then accepted H_2O concentrations are probably low in olivine, orthopyroxene and clinopyroxene standards and high in garnet. We note that there has been some recent discussion of appropriate quantification of H_2O in olivine from FTIR spectra (Bell et al. 2003; Koga et al. 2003). However, application of alternative FTIR calibrations for olivine, such as that of Paterson (1982) and Libowitzky and Rossman (1997) would result in lower accepted concentrations of H_2O in olivine and therefore cause greater discrepancies in interphase FTIR/SIMS calibration slopes.

To test whether the mineral-specific FTIR absorption schemes adopted in this study are the cause of apparent interphase FTIR/SIMS slope differences, we also quantified the H_2O in nominally anhydrous minerals using the methods of Libowitzky and Rossman (1997). In this FTIR absorption scheme, molar absorption coefficients are independent of mineral phase and depend only on wavenumber. As shown in Figure 9, H_2O concentrations of orthopyroxenes inferred from the Libowitzky and Rossman (1997) scheme are similar to those from the phase specific scheme of Bell et al. (1995). However, their concentrations for olivines, clinopyroxenes and garnets are lower than those derived from the procedures of Bell et al. (1995) and Bell et al. (2003). Thus, application of the scheme of Libowitzky and Rossman (1997) reduces the discrepancy between FTIR/SIMS calibrations of garnets and basaltic and rhyolitic glasses, but increases the discrepancies between the glasses and olivine and clinopyroxene. Whereas further work is needed to improve certainty in FTIR quantification of H in nominally anhydrous minerals, we conclude that the principal cause of interphase differences in FTIR/SIMS calibration slopes is not likely to be inaccuracies in FTIR absorption schemes.

A second possibility is that the intensities of ^1H and/or ^{30}Si negative secondary ions produced by Cs^+ beams are dependent on the structure or bonding environment of the target. Such effects may potentially arise owing to differences in bond strengths. Structure-dependent effects for O isotope ratios determined by SIMS using Cs^+ beams were documented by Eiler et al. (1997), who found different $^{18}O/^{16}O$ fractionation factors for minerals and glasses of the same composition. However, the differences owing to phase structure found by Eiler et al. (1997) amounted to fractionation factors of a few per mil, which are much smaller effects than the factor of 4 differences in FTIR/SIMS calibration slopes found for $^1H/^{30}Si$.

CONCLUDING REMARKS

Extensive intercalibration of FTIR and SIMS measurements demonstrates the reliability of SIMS for routine analysis of H in nominally anhydrous minerals. With appropriate steps to reduce the hydrogen background during analysis and careful calibration against well-characterized standards, SIMS analysis using Cs^+ beams and negative ions provide results that are comparable in precision and accuracy to FTIR down to at least 10 ppm H_2O. We observe small intraphase matrix effects, but substantial variations in SIMS/FTIR calibration slopes for different phases. The origin of such interphase variations are unknown, but may be related to inaccuracies in phase-specific FTIR calibrations or to structure-dependent behavior of samples. Until a better understanding of the origin of interphase calibration differences is achieved, analysis of H in nominally anhydrous minerals using Cs^+ and negative ions requires calibration against mineral-specific working curves.

The mode of hydrogen incorporation in many nominally anhydrous minerals is complex, with a wide variety of intrinsic (lattice bound hydrogen) and extrinsic (e.g., foreign phases) hydrous substitutions. These present complications for quantification of lattice bound hydrogen and challenges for intercalibration of FTIR and SIMS, which may sample different proportions of these hydrous substitutions. In many cases (though not all), experimentally annealed crystals present fewer problems for intercalibration than natural crystals. Owing to these complications, resolving the proportionality between FTIR and SIMS measurements of hydrogen in NAMs is greatly aided by the availability of a large number of calibration samples.

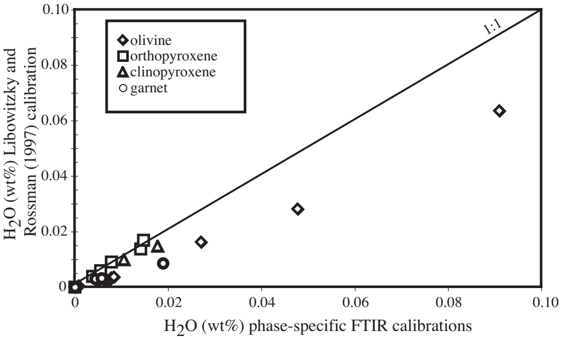

FIGURE 9. Comparison of H_2O content determined using the calibrations of Bell et al. (1995) and Bell et al. (2003) (horizontal axis) with those determined using the calibration of Libowitzky and Rossman (1997) (vertical axis).

ACKNOWLEDGMENTS

We are particularly grateful to Erik Hauri for introducing us to many of the SIMS techniques that we have pursued in this work. We thank R. Dasgupta for providing the Red Hill Cinder Cone rhyolitic glass, E. Hauri for donating the ALV519-4-1 basaltic glass. H. Behrens for sharing his rhyolitic glasses, and P. Ihinger (at University of Wisconsin, Eau Claire) for access to his infrared spectroscope. C. Chopin is thanked for providing the Dora Maira pyrope to A.C.W. We thank Emi Ito (U. of Minnesota) for the natural basaltic glasses used in this study and Mark Zimmermann and D. L. Kohlstedt for providing various starting materials. J. Eiler and G. Rossman are acknowledged for constructive reviews and P. Asimow for editorial handling. This work was supported by NASA under CAN-NCC5-679 (S. Mackwell) and NSF grant EAR0456405 to M. Hirschmann and L. Leshin. This paper is LPI contribution no. 1306.

REFERENCES CITED

Agrinier, P. and Jendrzejewski, N. (2000) Overcoming problems of density and thickness measurements in FTIR volatile determinations: a spectroscopic approach. Contributions to Mineralogy and Petrology, 139, 265–272.

Aines, R.D. and Rossman, G.R. (1984) Water content of mantle garnets. Geology, 12, 720–723.

Asimow, P.D., Dixon, J.E., and Langmuir, C.H. (2004) A hydrous melting and fractionation model for mid-ocean ridge basalts: application to the Mid-Atlantic Ridge near the Azores. Geochemistry Geophysics Geosystems, 5(1), 1–24 DOI:10.1029/2003GC000568.

Asimow, P.D., Stein, L.C., Mosenfelder, J.L., and Rossman, G.R. (2006) Quantitative polarized infrared analysis of trace OH in populations of randomly oriented mineral grains. American Mineralogist, 91, 278–284.

Bai, Q. and Kohlstedt, D.L. (1992) Substantial hydrogen solubility in olivine and implications for water storage in the mantle. Nature, 357, 672–674.

——— (1993) Effects of chemical environment on the solubility and incorporation mechanism for hydrogen in olivine. Physics and Chemistry of Minerals, 19, 460–471.

Bell, D.R. (1992) Water in mantle minerals. Nature, 357, 646–647.

Bell, D.R., Ihinger, P.D., and Rossman, G.R. (1995) Quantitative analysis of trace OH in garnet and pyroxenes. American Mineralogist, 80, 465–474.

Bell, D.R., Rossman, G.R., Maldener, J., Endisch, D., and Rauch, F. (2003) Hydroxide in olivine: a quantitative determination of the absolute amount and calibration of the IR spectrum. Journal of Geophysical Research, 108(B2), DOI: 10.1029/2001JB000679.

Bell, D.R., Rossman, G.R., and Moore, R.O. (2004) Abundance and partitioning of OH in a high-pressure magmatic system: megacrysts from the Monastery kimberlite, South Africa. Journal of Petrology, 45(8), 1539–1564.

Beran, A. and Putnis, A. (1983) A model of the OH positions in olivine, derived from infrared-spectroscopic investigations. Physics and Chemistry of Minerals, 9, 57–60.

Berman, R.G. and Koziol, A.M. (1991) Ternary excess properties of grossular-pyrope-almandine garnet and their influence in geothermobarometry. American Mineralogist, 76, 1223–1231.

Berry, A.J., Hermann, J., O'Neill, H.S.C., and Foran, G.J. (2005) Fingerprinting the water site in mantle olivine. Geology, 33, 869–872.

Blanchard, M. and Ingrin, J. (2004) Kinetics of deuteration in pyrope. European Journal of Mineralogy, 16, 567–576.

Bond, F.C. (1951) The third theory of comminution. Meeting of AIME in Mexico City, October 1951 in Mining Engineering, May 1952, 484–494.

Bromiley, G.D., Keppler, H., McCammon, C., Bromiley, F.A., and Jacobsen, S.D. (2004) Hydrogen solubility and speciation in natural, gem quality chromian diopside. American Mineralogist, 89, 941–949.

Bryan, W.B. and Moore, J.G. (1977) Compositional variations of young basalts in the Mid-Atlantic Ridge rift valley near lat 36°49'N. Geological Society of America Bulletin, 88, 556–570.

Chopin, C. (1984) Coesite and pure pyrope in high-grade blueschists of the Western Alps: a first record and some consequences. Contributions to Mineralogy and Petrology, 86, 107–-118.

Deloule, E., Paillat, O., Pichavant, M., and Scaillet, B. (1995) Ion microprobe determination of water in silicate glasses: methods and applications. Chemical Geology, 125, 19–28.

Dobson, P.F., Epstein, S., and Stolper, E.M. (1989) Hydrogen isotope fractionation between coexisting vapor and silicate glasses and melts at low pressure. Geochimica et Cosmochimica Acta, 53, 2723–2730.

Eiler, J.M., Graham, C., and Valley, J.W. (1997) SIMS analysis of oxygen isotopes: matrix effects in complex minerals and glasses. Chemical Geology, 138, 221–244.

Fine, G. and Stolper, E. (1985/1986) Dissolved carbon dioxide in basaltic glasses: concentrations ans speciation. Earth and Planetary Science Letters, 76, 263–278.

Fisher, G.W. and Medaris, L.G. (1969) Cell dimensions and X-ray determinative curve for synthetic Mg-Fe olivines. American Mineralogist, 54, 741–753.

Freund, F. and Oberheuser, G. (1986) Water dissolved in olivine: a single-crystal infrared study. Journal of Geophysical Research, 91(B1), 745–761.

Hauri, E.H., Wang, J., Dixon, J.E., King, P.L., Mandeville, C., and Newman, S. (2002) SIMS analysis of volatiles in silicate glasses 1. Calibration, matrix effects and comparisons with FTIR. Chemical Geology, 183, 99–114.

Hawthorne, F.C., Welch, M.D., Ventura, G.D., Liu, S., Robert, J.-L., and Jenkins, D.M. (2000) Short-range order in synthetic aluminous tremolites: An infrared and triple-quantum MAS NMR study. American Mineralogist, 85, 1716–1724.

Hinthorne, J.R. and Andersen, C.A. (1975) Microanalysis for fluorine and hydrogen in silicates with the ion microprobe mass analyser. American Mineralogist, 60, 143–147.

Hirschmann, M.M. (2006) Water, melting, and the deep Earth cycle. Annual Review of Earth and Planetary Sciences, 34, 629–653.

Hirth, G. and Kohlstedt, D.L. (1995) Experimental constraints on the dynamics of the partially molten upper mantle 2. Deformation in the dislocation creep regime. Journal of Geophysical Research, 100(B8), 15441–15449.

——— (1996) Water in the oceanic upper mantle: implications for rheology, melt extraction and the evolution of the lithosphere. Earth and Planetary Science Letters, 144, 93–108.

Huang, X., Xu, Y., and Karato, S.-I. (2005) Water content in the transition zone from electrical conductivity of wadsleyite and ringwoodite. Nature, 434, 746–749.

Ihinger, P.D., Hervig, R.L., and McMillan, P.F. (1994) Analytical methods for volatiles in glasses. In M.R. Carroll and J.R. Holloway, Ed., Volatiles in magmas, 30, 67–121. Reviews in Mineralogy, Mineralogical Society of America, Chantilly, Virginia.

Ingrin, J., Latrous, K., Doukhan, J.-C., and Doukhan, N. (1989) Water in diopside: an electron microscopy and infrared spectroscopy study. European Journal of Mineralogy, 1, 327–341.

Ishida, K. and Hawthorne, F.C. (2001) Assignment of infrared OH-stretching bands in manganoan-arfvedsonite and richterite through heat-treatment. American Mineralogist, 86, 965–972.

Jarosewich, E., Nelen, J.A., and Norberg, J.A. (1980) Reference samples for electron microprobe analysis. Geostandards Newsletter, 4, 43–47.

Jendrzejewski, N., Javoy, M., and Trull, T. (1996) Mesures quantitatives de carbone et d'eau dans les verres basaltiques naturels par spectroscopie infrarouge. Partie II: l'eau. Comptes Rendus de l'Académie des Sciences, 322(série IIa), 735–742.

Karato, S. (1990) The role of hydrogen in the electrical conductivity of the upper mantle. Nature, 347, 272–273.

Karato, S.-I. and Jung, H. (1998) Water, partial melting and the origin of the seismic low velocity and high attenuation zone in the upper mantle. Earth and Planetary Science Letters, 157, 193–207.

Katayama, I., Jung, H., and Karato, S.-I. (2004) New type of olivine fabric from deformation experiments at modest water content and low stress. Geology, 32(12), 1045–1048.

Khisina, N.R. and Wirth, R. (2002) Hydrous olivine $(Mg_{1-y}Fe_{2+y})_{2-x}V_xSiO_4H_{2x}$—a new DHMS phase of variable composition observed as nanometer-sized precipitations in mantle olivine. Physics and Chemistry of Minerals, 29, 98–111.

King, P.L., Vennemann, T.W., Holloway, J.R., Hervig, R.L., Lowenstern, J.B., and Forneris, J.F. (2002) Analytical techniques for volatiles: A case study using intermediate (andesitic glasses). American Mineralogist, 87, 1077–1089.

Kitamura, M., Kondoh, S., Morimoto, N., Miller, G.H., Rossman, G.R., and Putnis, A. (1987) Planar OH-bearing defects in mantle olivine. Nature, 328, 143–145.

Koga, K., Hauri, E., Hirschmann, M.M., and Bell, D. (2003) Hydrogen concentration analyses using SIMS and FTIR: comparison and calibration for nominally anhydrous minerals. Geochemistry Geophysics Geosystems, 4(2), DOI: 10.1029/2002GC000378.

Kohlstedt, D.L., Keppler, H., and Rubie, D.C. (1996) Solubility of water in the a, b and g phases of (Mg, Fe)$_2$SiO$_4$. Contributions to Mineralogy and Petrology, 123, 345–357.

Kohn, S.C. (1996) Solubility of H_2O in nominally anhydrous mantle minerals using 1H MAS NMR. American Mineralogist, 81, 1523–1526.

Kubo, T., Ohtani, E., Kato, T., Shinmei, T., and Fujino, K. (1998) Effects of water on the a-b transformation kinetics in San Carlos olivine. Science, 281, 85–87.

Lemaire, C., Kohn, S.C., and Brooker, R.A. (2004) The effect of silica activity on the incorporation mechanisms of water in synthetic forsterite: a polarised infrared spectroscopic study. Contributions to Mineralogy and Petrology, 147, 48–57.

Libowitzky, E. and Rossman, G.R. (1996) Principles of quantitative absorbance measurements in anisotropic crystals. Phys. Chem. Minerals, 23, 319–327.

——— (1997) An IR absorption calibration for water in minerals. American Mineralogist, 82, 1111–1115.

Lu, R. and Keppler, H. (1997) Water solubility in pyrope to 100 kbar. Contributions to Mineralogy and Petrology, 129, 35–42.

Mackwell, S., Dimos, D., and Kohlstedt, D.L. (1988) Transient creep of olivine: point defect relaxation times. Philosophical Magazine A, 57, 779–789.

Maldener, J., Hösch, A., Langer, K., and Rauch, F. (2003) Hydrogen in some natural garnets studied by nuclear reaction analysis and vibrational spectroscopy. Physics and Chemistry of Minerals, 30, 337–344.

Matsyuk, S.S. and Langer, K. (2004) Hydroxyl in olivines from mantle xenoliths in kimberlites of the Siberian platform. Contributions to Mineralogy and Petrology, 147, 413–437.

Matveev, S., O'Neill, H.S.C., Ballhaus, C., Taylor, W.R., and Green, D.H. (2001) Effect of silica activity on OH-IR spectra of olivine: implications for low-aSiO$_2$ mantle metasomatism. Journal of Petrology, 42, 721–729.

Miller, G.H., Rossman, G.R., and Harlow, G.E. (1987) The natural occurence of hydroxide in olivine. Physics and Chemistry of Minerals, 14, 461–472.

Miyashiro, A., Shido, F., and Ewing, M. (1969) Diversity and origin of abyssal tholeiite from the mid-Atlantic ridge near 24° and 30° North latitude. Contributions to Mineralogy and Petrology, 23, 38–52.

Nafziger, R.H. and Muan, A. (1967) Equilibrium phase compositions and thermodynamic properties of olivines and pyroxenes in the system MgO-"FeO"-SiO$_2$. American Mineralogist, 52, 1364–1385.

Ohlhorst, S., Behrens, H., and Holtz, F. (2001) Compositional dependence of molar absorptivities of near-infrared OH^- and H_2O bands in rhyolitic to basaltic glasses. Chemical Geology, 174, 5–20.

Parman, S. and Grove, T. (2004) Harzburgite melting with and without H_2O: experimental data and predictive modeling. Journal of Geophysical Research, 109, DOI: 10.1029/2003JB002566.

Paterson, M.S. (1982) The determination of hydroxyl by infrared absorption in quartz, silicate glasses and similar materials. Bulletin de Mineralogie, 105, 20–29.

Peslier, A.H., Luhr, J.F., and Post, J. (2002) Low water contents in pyroxenes from spinel-peridotites of the oxidized, sub-arc mantle wedge. Earth and Planetary Science Letters, 201, 69–86.

Rossman, G.R., Beran, A., and Langer, K. (1989) The hydrous component of pyrope from the Dora Maira Massif, Western Alps. European Journal of Mineralogy, 1, 151–154.

Sack, R.O. and Ghiorso, M.S. (1994) Thermodynamics of multicomponent pyroxenes; I. Formulation of a general model. Contributions to Mineralogy and Petrology, 116, 277–286.

Skogby, H., Bell, D.R., and Rossman, G.R. (1990) Hydroxide in pyroxene: variations in the natural environment. American Mineralogist, 75, 764–774.

Sobolev, A. and Chaussidon, M. (1996) H_2O concentrations in primary melts from supra-subduction zones and mid-ocean ridges: implications for H_2O storage and recycling in the mantle. Earth and Planetary Science Letters, 137, 45–55.

Stalder, R. (2004) Influence of Fe, Cr and Al on hydrogen incorporation in orthopyroxene. European Journal of Mineralogy, 16, 703–711.

Stolper, E.M. (1982) The speciation of water in silicate melts. Geochimica et Cosmochimica Acta, 46, 2609–2620.

Suzuki, T., Akaogi, M., and Yagi, T. (1996) Pressure dependence of Ni, Co and Mn partitioning between iron hydride and olivine, magnesiowüstite and pyroxene. Physics of the Earth and Planetary Interiors, 96, 209–220.

Sweeney, R.J., Prozesky, V.M., and Springhorn, K.A. (1997) Use of the elastic recoil detection analysis (ERDA) microbeam technique for the quantitative determination of hydrogen in materials and hydrogen partitioning between olivine and melt at high pressures. Geochimica et Cosmochimica Acta, 61, 101–113.

Wang, L., Zhang, Y., and Essene, E.J. (1996) Diffusion of the hydrous component in pyrope. American Mineralogist, 81, 706–718.

Wang, L., Essene, E.J., and Zhang, Y. (1999) Mineral inclusions in pyrope crustals from Garnet Ridge, Arizona, USA: implications for processes in the upper mantle. Contributions to Mineralogy and Petrology, 135, 164–178.

Wang, Z., Hiraga, T., and Kohlstedt, D.L. (2004) Effect of H^+ on Fe–Mg interdiffusion in olivine, $(Fe, Mg)_2SiO_4$. Applied Physics Letters, 85, 209–211.

Wiser, N.M. and Wood, B.J. (1991) Experimental determination of activities in Fe–Mg olivine at 1400 K. Contributions to Mineralogy and Petrology, 108, 146–153.

Withers, A.C., and Behrens, H. (1999) Temperature-induced changes in the NIR spectra of hydrous albitic and rhyolitic glasses between 300 and 100 K. Physics and Chemistry of Minerals, 27, 119–132.

Wood, B.J. (1995) The effect of H_2O on the 410-kilometer seismic discontinuity. Science, 268, 74–76.

Xirouchakis, D., Hirschmann, M.M., and Simpson, J.A. (2001) The effect of titanium on the silica content and on mineral-liquid partitioning of mantle-equilibrated melts. Geochimica et Cosmochimica Acta, 65, 2201–2217.

Yamashita, S., Kitamura, T., and Kusakabe, M. (1997) Infrared spectroscopy of hydrous glasses of arc magma compositions. Geochemical Journal, 31, 169–174.

Yurimoto, H., Kurosawa, M., and Sueno, S. (1989) Hydrogen analysis in quartz crystals and quartz glasses by secondary ion mass spectrometry. Geochimica et Cosmochimica Acta, 53, 751–755.

Zhao, Y.-H., Ginsberg, S.B., and Kohlstedt, D.L. (2004) Solubility of hydrogen in olivine: dependence on temperature and iron content. Contributions to Mineralogy and Petrology, 147, 155–161.

Manuscript received February 27, 2006
Manuscript accepted December 14, 2006
Manuscript handled by Paul Asimow